

1

²A SEARCH FOR LONG-LIVED, CHARGED, SUPERSYMMETRIC PARTICLES
³USING IONIZATION WITH THE ATLAS DETECTOR

4

BRADLEY AXEN

5

September 2016 – Version 0.32

6



⁸ Bradley Axen: *A Search for Long-Lived, Charged, Supersymmetric Particles using*
⁹ *Ionization with the ATLAS Detector*, Subtitle, © September 2016

¹⁰

Usually a quotation.

¹¹

Dedicated to.

₁₂ ABSTRACT

₁₃ How to write a good abstract:

₁₄ <https://plg.uwaterloo.ca/~migod/research/beck00PSLA.html>

₁₅ PUBLICATIONS

₁₆ Some ideas and figures have appeared previously in the following publications:

₁₇

₁₈ Put your publications from the thesis here. The packages `multibib` or `bibtopic`
₁₉ etc. can be used to handle multiple different bibliographies in your document.

²¹ ACKNOWLEDGEMENTS

²² Put your acknowledgements here.

²³

²⁴ And potentially a second round.

²⁵

26 CONTENTS

27	I	INTRODUCTION	1
28	1	INTRODUCTION	3
29	II	THEORETICAL CONTEXT	5
30	2	STANDARD MODEL	7
31	2.1	Particles	7
32	2.2	Interactions	8
33	2.3	Limitations	8
34	3	SUPERSYMMETRY	9
35	3.1	Motivation	9
36	3.2	Structure	9
37	3.3	Phenomenology	9
38	4	LONG-LIVED PARTICLES	11
39	4.1	Mechanisms	11
40	4.1.1	Examples in Supersymmetry	11
41	4.2	Phenomenology	11
42	4.2.1	Disimilarities to Prompt Decays	11
43	4.2.2	Characteristic Signatures	11
44	III	EXPERIMENTAL STRUCTURE AND RECONSTRUCTION	13
45	5	THE LARGE HADRON COLLIDER	15
46	5.1	Injection Chain	15
47	5.2	Design and Parameters	15
48	5.3	Luminosity	15
49	6	THE ATLAS DETECTOR	17
50	6.1	Coordinate System	17
51	6.2	Magnetic Field	17
52	6.3	Inner Detector	17
53	6.3.1	Pixel Detector	17
54	6.3.2	Semiconductor Tracker	17
55	6.3.3	Transition Radiation Tracker	17
56	6.4	Calorimetry	17
57	6.4.1	Electromagnetic Calorimeters	17
58	6.4.2	Hadronic Calorimeters	17
59	6.4.3	Forward Calorimeters	17
60	6.5	Muon Spectrometer	17
61	6.6	Trigger	17
62	6.6.1	Trigger Scheme	17
63	6.6.2	Missing Transverse Energy Triggers	17
64	7	EVENT RECONSTRUCTION	19
65	7.1	Tracks and Vertices	19

66	7.1.1	Track Reconstruction	19
67	7.1.2	Vertex Reconstruction	19
68	7.2	Jets	19
69	7.2.1	Topological Clustering	19
70	7.2.2	Jet Energy Scale	19
71	7.2.3	Jet Energy Scale Uncertainties	19
72	7.2.4	Jet Energy Resolution	19
73	7.3	Electrons	19
74	7.3.1	Electron Identification	19
75	7.4	Muons	19
76	7.4.1	Muon Identification	19
77	7.5	Missing Transverse Energy	19
78	IV	CALORIMETER RESPONSE	21
79	8	RESPONSE MEASUREMENT WITH SINGLE HADRONS	23
80	8.1	Dataset and Simulation	24
81	8.1.1	Data Samples	24
82	8.1.2	Simulated Samples	24
83	8.1.3	Event Selection	24
84	8.2	Inclusive Hadron Response	25
85	8.2.1	E/p Distribution	26
86	8.2.2	Zero Fraction	26
87	8.2.3	Neutral Background Subtraction	28
88	8.2.4	Corrected Response	28
89	8.3	Identified Particle Response	34
90	8.3.1	Decay Reconstruction	34
91	8.3.2	Identified Response	35
92	8.3.3	Additional Species in Simulation	37
93	8.4	Summary	38
94	9	JET ENERGY RESPONSE AND UNCERTAINTY	41
95	9.1	Motivation	41
96	9.2	Uncertainty Estimate	41
97	9.3	Summary	44
98	V	SEARCH FOR LONG-LIVED PARTICLES	47
99	10	LONG-LIVED PARTICLES IN ATLAS	49
100	10.1	Overview and Characteristics	49
101	10.2	Simulation	49
102	11	EVENT SELECTION	51
103	11.1	Trigger	52
104	11.2	Kinematics and Isolation	52
105	11.3	Standard Model Rejection	55
106	11.4	Ionization	58
107	11.4.1	Mass Estimation	58
108	11.5	Efficiency	59
109	12	BACKGROUND ESTIMATION	63

110	12.1	Background Sources	63
111	12.2	Prediction Method	64
112	12.3	Validation	65
113	12.3.1	Closure in Simulation	65
114	12.3.2	Validation Region in Data	66
115	13	SYSTEMATIC UNCERTAINTIES AND RESULTS	69
116	13.1	Systematic Uncertainties	69
117	13.2	Final Yields	69
118	14	INTERPRETATION	71
119	14.1	Cross Sectional Limits	71
120	14.2	Mass Limits	71
121	14.3	Context for Long-Lived Searches	71
122	VI	CONCLUSIONS	73
123	15	SUMMARY AND OUTLOOK	75
124	15.1	Summary	75
125	15.2	Outlook	75
126	VII	APPENDIX	77
127	A	INELASTIC CROSS SECTION	79
128	B	APPENDIX TEST	81
129	B.1	Appendix Section Test	81
130	B.1.1	Appendix Subection Test	81
131	B.2	A Table and Listing	81
132	B.3	Some Formulas	82
133	BIBLIOGRAPHY		85

134 LIST OF FIGURES

135	Figure 1	The particle content of the Standard Model (SM).	8
136	Figure 2	An illustration (a) of the E/p variable used throughout this paper. The red energy deposits come from the charged particle targeted for measurement, while the blue energy deposits are from nearby neutral particles and must be subtracted. The same diagram (b) for the neutral-background selection, described in Section 8.2.3.	25
137			
138			
139			
140			
141			
142	Figure 3	The E/p distribution and ratio of simulation to data for isolated tracks with (a) $ \eta < 0.6$ and $1.2 < p/\text{GeV} < 1.8$ and (b) $ \eta < 0.6$ and $2.2 < p/\text{GeV} < 2.8$	26
143			
144			
145	Figure 4	The fraction of tracks as a function (a, b) of momentum, (c, d) of interaction lengths with $E \leq 0$ for tracks with positive (on the left) and negative (on the right) charge.	27
146			
147			
148			
149	Figure 5	$\langle E/p \rangle_{\text{BG}}$ as a function of the track momentum for tracks with (a) $ \eta < 0.6$, (b) $0.6 < \eta < 1.1$, and as a function of the track pseudorapidity for tracks with (c) $1.2 < p/\text{GeV} < 1.8$, (d) $1.8 < p/\text{GeV} < 2.2$	29
150			
151			
152			
153	Figure 6	$\langle E/p \rangle_{\text{COR}}$ as a function of track momentum, for tracks with (a) $ \eta < 0.6$, (b) $0.6 < \eta < 1.1$, (c) $1.8 < \eta < 1.9$, and (d) $1.9 < \eta < 2.3$	30
154			
155			
156	Figure 7	$\langle E/p \rangle_{\text{COR}}$ calculated using LCW-calibrated topological clusters as a function of track momentum for tracks with (a) zero or more associated topological clusters or (b) one or more associated topological clusters.	31
157			
158			
159			
160	Figure 8	Comparison of the $\langle E/p \rangle_{\text{COR}}$ for tracks with (a) less than and (b) greater than 20 hits in the TRT.	32
161			
162	Figure 9	Comparison of the $\langle E/p \rangle_{\text{COR}}$ for (a) positive and (b) negative tracks as a function of track momentum for tracks with $ \eta < 0.6$	32
163			
164			
165	Figure 10	Comparison of the E/p distributions for (a) positive and (b) negative tracks with $0.8 < p/\text{GeV} < 1.2$ and $ \eta < 0.6$, in simulation with the FTFP_BERT and QGSP_BERT physics lists.	33
166			
167			
168			
169	Figure 11	Comparison of the response of the hadronic calorimeter as a function of track momentum (a) at the EM-scale and (b) after the LCW calibration.	33
170			
171			
172	Figure 12	Comparison of the response of the EM calorimeter as a function of track momentum (a) at the EM-scale and (b) with the LCW calibration.	34
173			
174			

175	Figure 13	The reconstructed mass peaks of (a) K_S^0 , (b) Λ , and (c) $\bar{\Lambda}$ candidates.	35
176			
177	Figure 14	The E/p distribution for isolated (a) π^+ , (b) π^- , (c) proton, and (d) anti-proton tracks.	36
178			
179	Figure 15	The fraction of tracks with $E \leq 0$ for identified (a) π^+ and π^- , and (b) proton and anti-proton tracks	36
180			
181	Figure 16	The difference in $\langle E/p \rangle$ between (a) π^+ and π^- (b) p and π^+ , and (c) \bar{p} and π^-	37
182			
183	Figure 17	$\langle E/p \rangle_{\text{COR}}$ as a function of track momentum for (a) π^+ tracks and (b) π^- tracks.	38
184			
185	Figure 18	The ratio of the calorimeter response to single parti- cles of various species to the calorimeter response to π^+ with the physics list FTFP_BERT.	38
186			
187	Figure 19	The spectra of true particles inside anti- k_t , $R = 0.4$ jets with (a) $90 < p_T/\text{GeV} < 100$, (b) $400 < p_T/\text{GeV} <$ 500 , and (c) $1800 < p_T/\text{GeV} < 2300$	42
188			
190	Figure 20	The jet energy scale (JES) uncertainty contributions, as well as the total JES uncertainty, as a function of jet p_T for (a) $ \eta < 0.6$ and (b) $0.6 < \eta < 1.1$	44
191			
193	Figure 21	The JES correlations as a function of jet p_T and $ \eta $ for jets in the central region of the detector.	45
194			
196	Figure 22	The distribution of E_T^{miss} for data and simulated signal events, after the trigger requirement.	53
197			
198	Figure 23	The dependence of dE/dx on N_{split} in data after basic track hit requirements have been applied.	54
199			
200	Figure 24	The distribution of dE/dx with various selections ap- plied in data and simulated signal events.	55
201			
202	Figure 25	The distribution of track momentum for data and sim- ulated signal events, after previous selection require- ments have been applied.	56
203			
204	Figure 26	The distribution of M_T for data and simulated sig- nal events, after previous selection requirements have been applied.	57
205			
207	Figure 27	The distribution of summed tracked momentum within a cone of $\Delta R < 0.25$ around the candidate track for data and simulated signal events, after previous selec- tion requirements have been applied.	58
208			
211	Figure 28	The normalized, two-dimensional distribution of E/p and f_{EM} for simulated (a) $Z \rightarrow ee$, (b) $Z \rightarrow \tau\tau$, (c) 1200 GeV Stable R-Hadron events, and (d) 1200 GeV, 10 ns R-Hadron events.	59
212			
214	Figure 29	Two-dimensional distribution of dE/dx versus charge signed momentum (qp) for minimum-bias tracks. The fitted distributions of the most probable values for pi- ons, kaons and protons are superimposed.	60
215			
216			
217			
218			
219			

220	Figure 30	The distribution of mass estimated using dE/dx for simulated stable R-Hadrons with masses between 1000 and 1600 GeV.	60
221			
222			
223	Figure 31	The acceptance \times efficiency as a function of R-Hadron (a) mass and (b) lifetime. (a) shows all of the combinations of mass and lifetime considered in this search, and (b) highlights the lifetime dependence for 1000 GeV and 1600 GeV R-Hadrons.	62
224			
225			
226			
227			
228	Figure 32	The distribution of (a) dE/dx and (b) momentum for tracks in data and simulated signal after requiring the event level selection and the track selection on p_T , hits, and N_{split} . Each sub-figure shows the normalized distributions for tracks classified as hadrons, electrons, and muons in data and R-Hadrons in the simulated signal.	64
229			
230			
231			
232			
233			
234			
235	Figure 33	The distribution of $M_{dE/dx}$ (a) before and (b) after the ionization requirement for tracks in simulated W boson decays and for the randomly generated background estimate.	66
236			
237			
238			
239	Figure 34	The distribution of $M_{dE/dx}$ (a) before and (b) after the ionization requirement for tracks in the validation region and for the randomly generated background estimate.	67
240			
241			
242			

243 LIST OF TABLES

255 LISTINGS

<small>256</small>	Listing 1	A floating example (<code>listings</code> manual)	82
--------------------	-----------	--	----

257 ACRONYMS

- 258 SM Standard Model
259 LSP Lightest Supersymmetric Particle
260 LHC Large Hadron Collider
261 ToT time over threshold
262 LCW local cluster weighted
263 MIP minimally ionizing particle
264 EPJC European Physical Journal C
265 JES jet energy scale
266 LLP Long-Lived Particle
267 CR Control Region

268

PART I

269

INTRODUCTION

270

You can put some informational part preamble text here.

1

271

272 INTRODUCTION

²⁷³

PART II

²⁷⁴

THEORETICAL CONTEXT

²⁷⁵

You can put some informational part preamble text here.

2

276

277 STANDARD MODEL

278 The SM of particle physics seeks to explain the symmetries and interactions of
279 all currently discovered fundamental particles. It has been tested by several genera-
280 tions of experiments and has been remarkably successful, no significant de-
281 viations have been found. The SM provides predictions in particle physics for
282 interactions up to the Planck scale (10^{15} - 10^{19} GeV).

283 The theory itself is a quantum field theory grown from an underlying $SU(3) \times$
284 $SU(2) \times U(1)$ that requires the particle content and quantum numbers consist-
285 ent with experimental observations (see Section 2.1). Each postulated symme-
286 try is accompanied by an interaction between particles through gauge invari-
287 ance. These interactions are referred to as the Strong, Weak, and Electromag-
288 netic forces, which are discussed in Section 2.2.

289 Although this model has been very predictive, the theory is incomplete; for
290 example, it is not able to describe gravity or astronomically observed dark matter.
291 These limitations are discussed in more detail in Section 2.3.

292 21 PARTICLES

293 The most familiar matter in the universe is made up of protons, neutrons, and
294 electrons. Protons and neutrons are composite particles, however, and are made
295 up in turn by particles called quarks. Quarks carry both electric charge and color
296 charge, and are bound in color-neutral combinations called baryons. The elec-
297 tron is an example of a lepton, and carries only electric charge. Another type
298 of particle, the neutrino, does not form atomic structures in the same way that
299 quarks and leptons do because it carries no color or electric charge. Collectively,
300 these types of particles are known as fermions, the group of particles with half-
301 integer spin.

302 There are three generations of fermions, although familiar matter is formed
303 predominantly by the first generation. The generations are identical except for
304 their masses, which increase in each generation by convention. In addition, each
305 of these particles is accompanied by an antiparticle, with opposite-sign quantum
306 numbers but the same mass.

307 The fermions comprise what is typically considered matter, but there are
308 additional particles that are mediators of interactions between those fermions.
309 These mediators are known as the gauge bosons, gauge in that their existence
310 is required by gauge invariance (discussed further in Section 2.2) and bosons in
311 that they have integer spin. The boson which mediates the electromagnetic force
312 is the photon, the first boson to be discovered; it has no electric charge, no mass,
313 and a spin of 1. There are three spin-1 mediators of the weak force, the two
314 W bosons and the Z boson. The W bosons have electric charge of ± 1 and a
315 mass of 80.385 ± 0.015 GeV, while the Z boson is neutral and has a mass of

316 91.1876 \pm 0.0021 GeV. The strong force is mediated by eight particles called
 317 gluons, which are massless and electrically neutral but do carry color charge.

318 The final particle present in the SM is the Higgs boson, which was recently
 319 observed for the first time by experiments at CERN in 2012. It is electrically
 320 neutral, has a mass of 125.7 \pm 0.4 GeV, and is the only spin-0 particle yet to be
 321 observed. The Higgs boson is the gauge boson associated with the mechanism
 322 that gives a mass to the W and Z bosons.

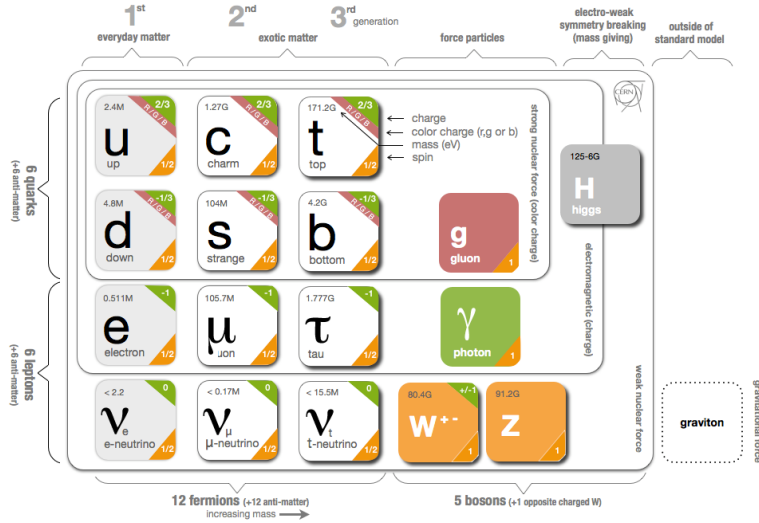


Figure 1: The particle content of the SM.

323 Together these particles form the entire content of the SM, and are summa-
 324 rized in Figure 1. These are the particles that constitute the observable universe
 325 and all the so-far-observed interactions within it.

326 2.2 INTERACTIONS

327 The interactions predicted and described by the SM are fundamentally tied to the
 328 particles within it, both in that they describe the way those particles can influence
 329 each other and also in that the existence of the interactions requires the existence
 330 of some particles (the gauge bosons).

331 2.3 LIMITATIONS

3

332

333 SUPERSYMMETRY

334 3.1 MOTIVATION

335 3.2 STRUCTURE

336 3.3 PHENOMENOLOGY

4

337

338 LONG-LIVED PARTICLES

339 4.1 MECHANISMS

340 4.1.1 EXAMPLES IN SUPERSYMMETRY

341 4.2 PHENOMENOLOGY

342 4.2.1 DISIMILARITIES TO PROMPT DECAYS

343 4.2.2 CHARACTERISTIC SIGNATURES

344

PART III

345

EXPERIMENTAL STRUCTURE AND RECONSTRUCTION

346

You can put some informational part preamble text here.

5

347

348 THE LARGE HADRON COLLIDER

349 5.1 INJECTION CHAIN

350 5.2 DESIGN AND PARAMETERS

351 5.3 LUMINOSITY

6

352

353 THE ATLAS DETECTOR

354 6.1 COORDINATE SYSTEM

355 6.2 MAGNETIC FIELD

356 6.3 INNER DETECTOR

357 6.3.1 PIXEL DETECTOR

358 6.3.2 SEMICONDUCTOR TRACKER

359 6.3.3 TRANSITION RADIATION TRACKER

360 6.4 CALORIMETRY

361 6.4.1 ELECTROMAGNETIC CALORIMETERS

362 6.4.2 HADRONIC CALORIMETERS

363 6.4.3 FORWARD CALORIMETERS

364 6.5 MUON SPECTROMETER

365 6.6 TRIGGER

366 6.6.1 TRIGGER SCHEME

367 6.6.2 MISSING TRANSVERSE ENERGY TRIGGERS

368

369 EVENT RECONSTRUCTION

370 The ATLAS experiment combines measurements in the subdetectors to form a
371 cohesive picture of each physics event.

372 7.1 TRACKS AND VERTICES

373 7.1.1 TRACK RECONSTRUCTION

374 7.1.1.1 NEURAL NETWORK

375 7.1.1.2 PIXEL DE/DX

376 7.1.2 VERTEX RECONSTRUCTION

377 7.2 JETS

378 7.2.1 TOPOLOGICAL CLUSTERING

379 7.2.2 JET ENERGY SCALE

380 7.2.3 JET ENERGY SCALE UNCERTAINTIES

381 7.2.4 JET ENERGY RESOLUTION

382 7.3 ELECTRONS

383 7.3.1 ELECTRON IDENTIFICATION

384 7.4 MUONS

385 7.4.1 MUON IDENTIFICATION

386 7.5 MISSING TRANSVERSE ENERGY

387

PART IV

388

CALORIMETER RESPONSE

389

You can put some informational part preamble text here.

391 RESPONSE MEASUREMENT WITH SINGLE HADRONS

392 As discussed in Section 7.2, colored particles produced in collisions hadronize
393 into jets of multiple hadrons. One approach to understanding jet energy mea-
394 surements in the ATLAS calorimeters is to evaluate the calorimeter response to
395 those individual hadrons; measurements of individual hadrons can be used to
396 build up an understanding of the jets that they form. The redundancy of the
397 momentum provided by the tracking system and the energy provided by the
398 calorimeter provides an opportunity to study calorimeter response using real
399 collisions, as described further in Section 8.2.

400 Calorimeter response includes a number of physical effects that can be ex-
401 tracted to provide insight into many aspects of jet modeling. First, many charged
402 hadrons interact with the material of the detector prior to reaching the calorime-
403 ters and thus do not deposit any energy. Comparing this effect in data and simu-
404 lation is a powerful tool in validating the interactions of particles with the mate-
405 rial of the detector and the model of the detector geometry in simulation, see Sec-
406 tion 8.2.2. The particles which do reach the calorimeter deposit their energy into
407 several adjacent cells, which are then clustered together. The energy of the clus-
408 ter is then the total energy deposited by that particle. Comparing the response of
409 hadrons in data to that of simulated hadrons provides a direct evaluation of the
410 showering of hadronic particles and the energy deposited by particles in matter
411 (Section 8.2.4).

412 The above studies all use an inclusive selection of charged particles, which are
413 comprised predominantly of pions, kaons, and (anti)protons. It is also possible to
414 measure the response to various identified particle types separately to evaluate
415 the simulated interactions of each particle, particularly at low energies where
416 differences between species are very relevant. Pions and (anti)protons can be
417 identified through decays of long-lived particles, in particular Λ , $\bar{\Lambda}$, and K_S^0 , and
418 then used to measure response as described above. This is discussed in detail in
419 Section 8.3.

420 Together, these measurements in data provide a thorough understanding of
421 the way hadrons interact with the ATLAS detector and can be used to build up a
422 description of jets, as seen in Chapter 9. The results in this chapter use data col-
423 lected at 7 and 8 TeV collected in 2010 and 2012, respectively. Both are included
424 as the calorimeter was repaired and recalibrated between those two data-taking
425 periods. Both sets of data are compared to an updated simulation that includes
426 new physics models provided by Geant4 [1] and improvements in the detec-
427 tor description [2, 3]. These results are published in European Physical Journal
428 C (EPJC) [4] and can be compared to a similar measurement performed in 2009
429 and 2010 [5], which used the previous version of the simulation framework [6].

430 8.1 DATASET AND SIMULATION

431 8.1.1 DATA SAMPLES

432 The two datasets used in this chapter are taken from dedicated low-pileup runs
 433 where the fraction of events with multiple interactions was negligible, to facilitate
 434 measurement of isolated hadrons. The 2012 dataset at $\sqrt{s} = 8$ TeV contains
 435 8 million events and corresponds to an integrated luminosity of 0.1 nb^{-1} . The
 436 2010 dataset at $\sqrt{s} = 7$ TeV contains 3 million events and corresponds to an
 437 integrated luminosity of 3.2 nb^{-1} . The latter dataset was also used in the 2010
 438 results [5], but it has since been reanalyzed with an updated detector description
 439 for the material and alignment.

440 8.1.2 SIMULATED SAMPLES

441 The two datasets above are compared to simulated single-, double-, and non-
 442 diffractive events generated with Pythia8 [7] using the A2 configuration of
 443 hadronization [8] and the MSTW 2008 parton-distribution function set [9, 10].
 444 The conditions and energies for each run are matched in the two simulations.

445 To evaluate the interaction of hadrons with detector material, the simulation
 446 uses two different collections of hadronic physics models, called physics lists, in
 447 Geant4 9.4 [11]. The first, QGSP_BERT, combines the Bertini intra-nuclear
 448 cascade [12–14] below 9.9 GeV, a parametrized proton inelastic model from 9.5
 449 to 25 GeV [15], and a quark-gluon string model above 12 GeV [16–20]. The
 450 second, FTFP_BERT, combines the Bertini intra-nuclear cascade [12–14] below
 451 5 GeV and the Fritiof model [21–24] above 4 GeV. In either list, Geant4 en-
 452 forces a smooth transition between models where multiple models overlap.

453 8.1.3 EVENT SELECTION

454 The event selection for this study is minimal, as the only requirement is selecting
 455 good-quality events with an isolated track. Such events are triggered by requir-
 456 ing at least two hits in the minimum-bias trigger scintillators. After trigger, each
 457 event is required to have exactly one reconstructed vertex, and that vertex is re-
 458 quired to have four or more associated tracks.

459 The particles which enter into the response measurements are first identified
 460 as tracks in the inner detector. The tracks are required to have at least 500 MeV
 461 of transverse momentum. To ensure a reliable momentum measurement, these
 462 tracks are required to have at least one hit in the pixel detector, six hits in the SCT,
 463 and small longitudinal and transverse impact parameters with respect to the pri-
 464 mary vertex [5]. For the majority of the measurements in this chapter, the track is
 465 additionally required to have 20 hits in the TRT, which significantly reduces the
 466 contribution from tracks which undergo nuclear interactions. This requirement
 467 and its effect is discussed in more detail in Section 8.2.4.1. In addition, tracks are
 468 rejected if there is another track which extrapolates to the calorimeter within a

cone of $\Delta R = \sqrt{(\Delta\phi)^2 + (\Delta\eta)^2} < 0.4$. This requirement guarantees that the contamination of energy from nearby charged particles is negligible [5].

8.2 INCLUSIVE HADRON RESPONSE

The calorimeter response is more precisely defined as the ratio of the measured calorimeter energy to the true energy carried by the particle, although this true energy is unknown. For charged particles, however, the inner detector provides a very precise measurement of momentum (with uncertainty less than 1%) that can be used as a proxy for true energy. The ratio of the energy deposited by the charged particle in the calorimeter, E , to its momentum measured in the inner detector p , forms the calorimeter response measure called E/p . Though the distribution of E/p contains a number of physical features, this study focuses on the trends in two aggregated quantities: $\langle E/p \rangle$, the average of E/p within a given subset of particles, and the zero fraction, the fraction of particles with no associated energy in the calorimeter.

The calorimeter energy assigned to a track particle is defined using clusters. The clusters are formed using a 4–2–0 algorithm [25] that begins with seeds requiring at least 4 times the average calorimeter noise. The neighboring cells with at least twice that noise threshold are then added to the cluster, and all bounding cells are then added with no requirement. This algorithm minimizes noise contributions through its seeding process, and including the additional layers improves the energy resolution [26]. The clusters are associated to a given track if they fall within a cone of $\Delta R = 0.2$ of the extrapolated position of the track, which includes about 90% of the energy on average [5]. This construction is illustrated in Figure 2.

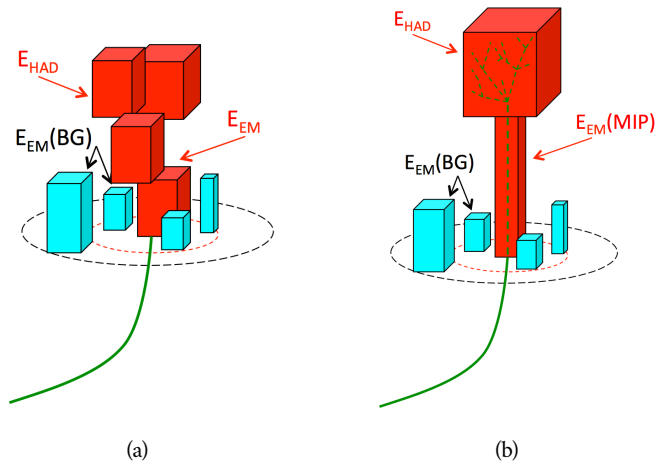


Figure 2: An illustration (a) of the E/p variable used throughout this paper. The red energy deposits come from the charged particle targeted for measurement, while the blue energy deposits are from nearby neutral particles and must be subtracted. The same diagram (b) for the neutral-background selection, described in Section 8.2.3.

493 8.2.1 E/P DISTRIBUTION

494 The E/p distributions measured in both data and simulation are shown in Figure 3 for two example bins of track momentum and for tracks in the central
 495 region of the detector. These distributions show several important features of
 496 the E/p observable. The large content in the bin at $E = 0$ comes from tracks
 497 that have no associated cluster, which occurs due to interactions with detector
 498 material prior to reaching the calorimeter or the energy deposit being insuffi-
 499 ciently large to generate a seed, and are discussed in Section 8.2.2. The small
 500 negative tail comes from similar tracks that do not deposit any energy in the
 501 calorimeter but are randomly associated to a noise cluster. The long positive
 502 tail above 1.0 comes from the contribution of neutral particles. Nearby neutral
 503 particles deposit (sometimes large) additional energy in the calorimeter but do
 504 not produce tracks in the inner detector, so they cannot be rejected by the track
 505 isolation requirement. Additionally the peak and mean of the distribution falls
 506 below 1.0 because of the loss of energy not found within the cone as well as the
 507 non-compensation of the calorimeter.

508 The data and simulation share the same features, but the high and low tails
 509 are significantly different. The simulated events tend to overestimate the con-
 510 tribution of neutral particles to the long tail, an effect which can be isolated and
 511 removed as discussed in Section 8.2.3. Additionally, the simulated clusters have
 512 less noise on average, although this is a small effect on the overall response.
 513

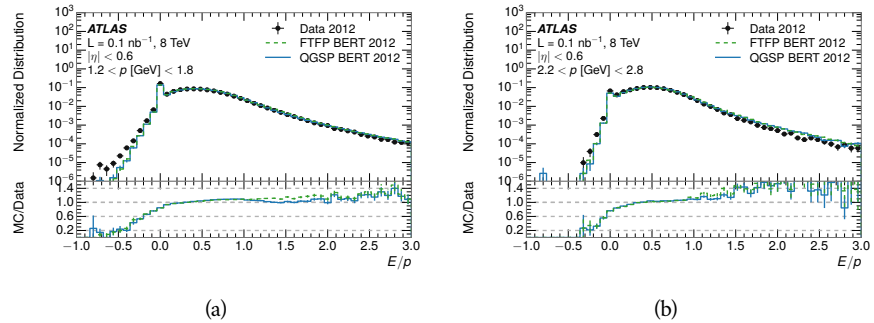


Figure 3: The E/p distribution and ratio of simulation to data for isolated tracks with
 (a) $|\eta| < 0.6$ and $1.2 < p/\text{GeV} < 1.8$ and (b) $|\eta| < 0.6$ and $2.2 < p/\text{GeV} < 2.8$.

514 8.2.2 ZERO FRACTION

515 The fraction of particles with no associated clusters, or similarly those with $E \leq$
 516 0, reflects the modeling of both the detector geometry and hadronic interactions.
 517 The zero fraction is expected to rise as the amount of material a particle traverses
 518 increases, while it is expected to decrease as the particle energy increases. This
 519 dependence can be seen in Figure 4, where the zero fraction in data and simula-
 520 tion is shown as a function of momentum and the amount of material measured
 521 in interaction lengths. The trends are similar between the 2010 and 2012 mea-
 522 surements. The zero fraction decreases with energy as expected. The amount of

material in the detector increases with η , which provides a distribution of interaction lengths. As the data and simulation have significant disagreement in the zero fraction over a number of interaction lengths, the difference must be primarily from the modeling of hadronic interactions with detector material and not just the detector geometry.

There is also a noticeable difference between positive and negative tracks at low momentum, which reflects the difference in response between protons and antiprotons. Antiprotons have significant model differences in the two physics lists, QGSP_BERT and FTFP_BERT, and this is evident in the lowest momentum bin of the data to simulation ratio. This difference is explored further in Section 8.3.

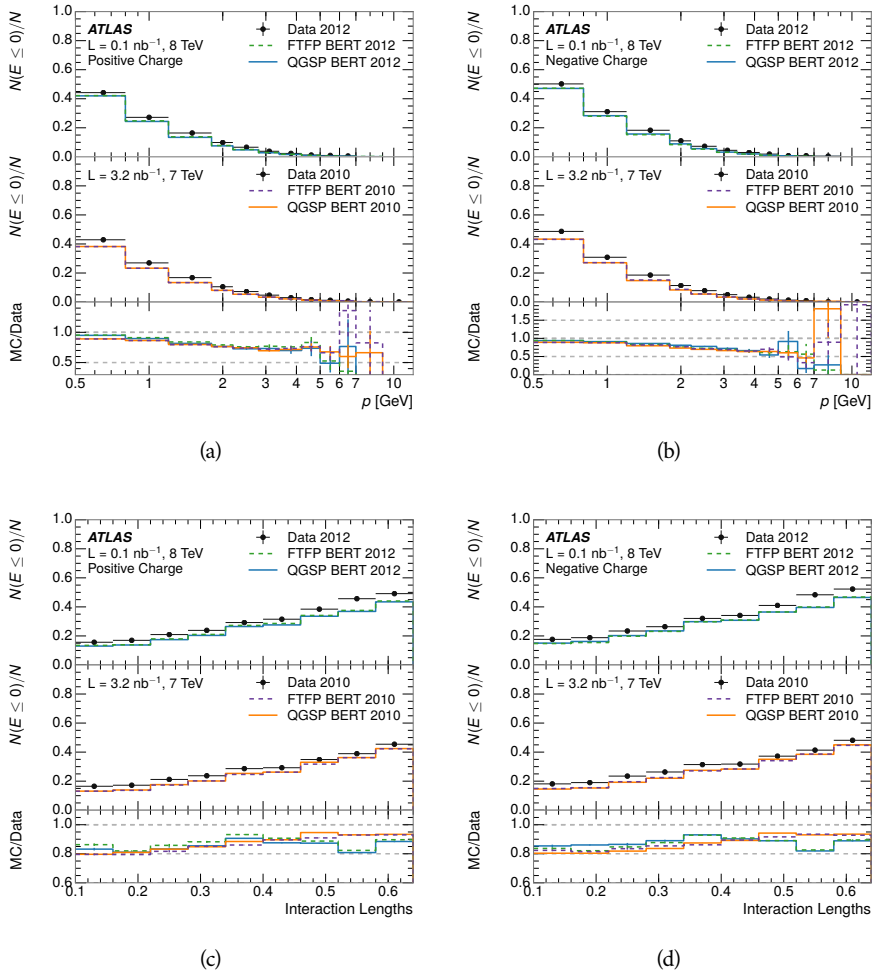


Figure 4: The fraction of tracks as a function (a, b) of momentum, (c, d) of interaction lengths with $E \leq 0$ for tracks with positive (on the left) and negative (on the right) charge.

534 8.2.3 NEUTRAL BACKGROUND SUBTRACTION

535 The isolation requirement on hadrons is only effective in remove energy contri-
 536 bution from nearby charged particles. Nearby neutral particles, predominantly
 537 photons from π^0 decays, also add their energy to the calorimeter clusters, but
 538 mostly in the electromagnetic calorimeter. It is possible to measure this contri-
 539 bution, on average, using late-showering hadrons that minimally ionize in the
 540 electromagnetic calorimeter. Such particles are selected by requiring that they
 541 deposit less than 1.1 GeV in the EM calorimeter within a cone of $\Delta R < 0.1$
 542 around the track. To ensure that these particles are well measured, they are addi-
 543 tionally required to deposit between 40% and 90% of their energy in the hadronic
 544 calorimeter within the same cone.

545 These particles provide a clean sample to measure the nearby neutral back-
 546 ground because they do not deposit energy in the area immediately surrounding
 547 them in the EM calorimeter, as shown in Figure 2. So, the energy deposits in the
 548 region $0.1 < \Delta R < 0.2$ can be attributed to neutral particles alone. To estimate
 549 the contribution to the whole cone considered for the response measurement,
 550 that energy is scaled by a geometric factor of 4/3. This quantity, $\langle E/p \rangle_{\text{BG}}$, mea-
 551 sured in aggregate over a number of particles, gives the contribution to $\langle E/p \rangle$
 552 from neutral particles in the EM calorimeter. Similar techniques were used in
 553 the individual layers of the hadronic calorimeters to show that the background
 554 from neutrals is negligible in those layers [5].

555 The distribution of this background estimate is shown in Figure 5. Although
 556 the simulation captures the overall trend, it significantly overestimates the neu-
 557 tral contribution for tracks with momentum between 2 and 8 GeV. This effect
 558 was also seen in the tails of the E/p distributions in Figure 3. This difference is
 559 likely due to the modeling of coherent neutral particle radiation in Pythia8, as
 560 the discrepancy does not depend on η and thus is unlikely to be a mismodeling
 561 of the detector. This difference can be subtracted to form a corrected average
 562 E/p , as in Section 8.2.4.

563 8.2.4 CORRECTED RESPONSE

564 Figure 6 shows $\langle E/p \rangle_{\text{COR}}$ as a function of momentum for several bins of pseu-
 565 dorapidity. This corrected $\langle E/p \rangle_{\text{COR}} \equiv \langle E/p \rangle - \langle E/p \rangle_{\text{BG}}$ measures the average
 566 calorimeter response without the contamination of neutral particles. It is the
 567 most direct measurement of calorimeter response in that it is the energy mea-
 568 sured for fully isolated hadrons. The correction is performed separately in data
 569 and simulation, so that the mismodeling of the neutral background in simulation
 570 is removed from the comparison of response. The simulation overestimates the
 571 response at low momentum by about 5%, an effect that can be mostly attributed
 572 to the underestimation of the zero fraction mentioned previously.

573 The response measurement above used topological clustering at the EM scale,
 574 that is clusters were formed to measure energy but no corrections were applied
 575 to correct for expected effects like energy lost outside of the cluster or in unin-
 576 strumented material. It is also interesting to measure $\langle E/p \rangle_{\text{COR}}$ using local clus-

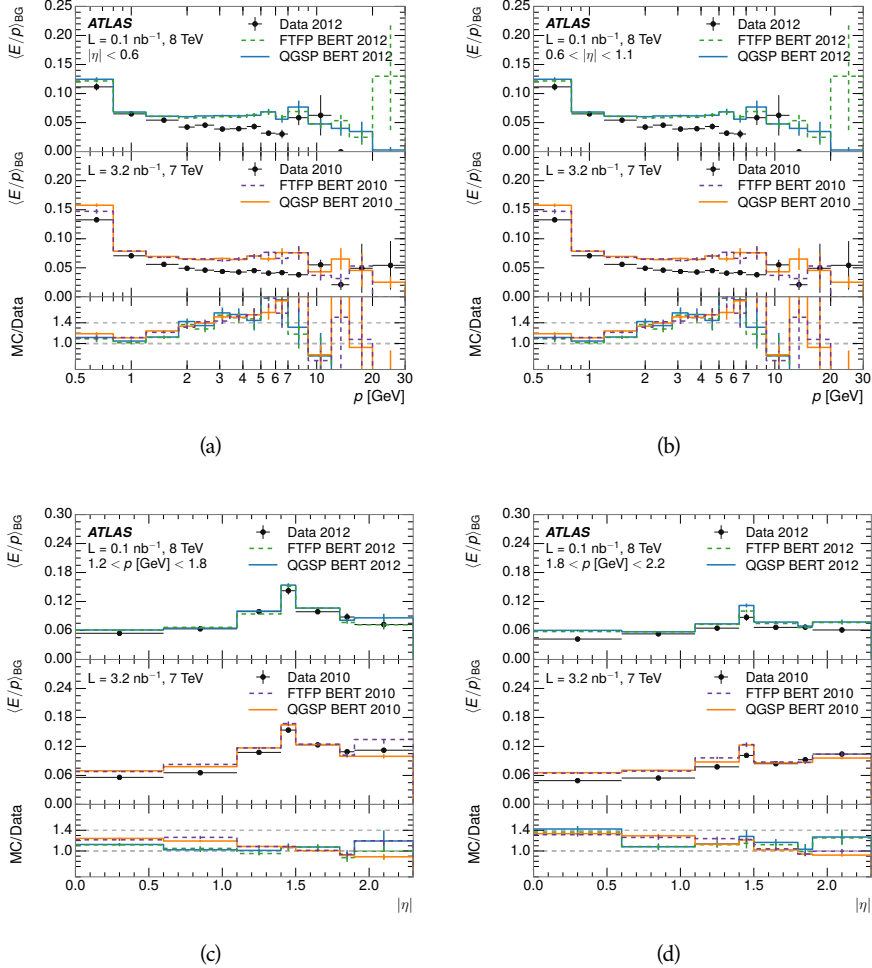


Figure 5: $\langle E/p \rangle_{\text{BG}}$ as a function of the track momentum for tracks with (a) $|\eta| < 0.6$, (b) $0.6 < |\eta| < 1.1$, and as a function of the track pseudorapidity for tracks with (c) $1.2 < p/\text{GeV} < 1.8$, (d) $1.8 < p/\text{GeV} < 2.2$.

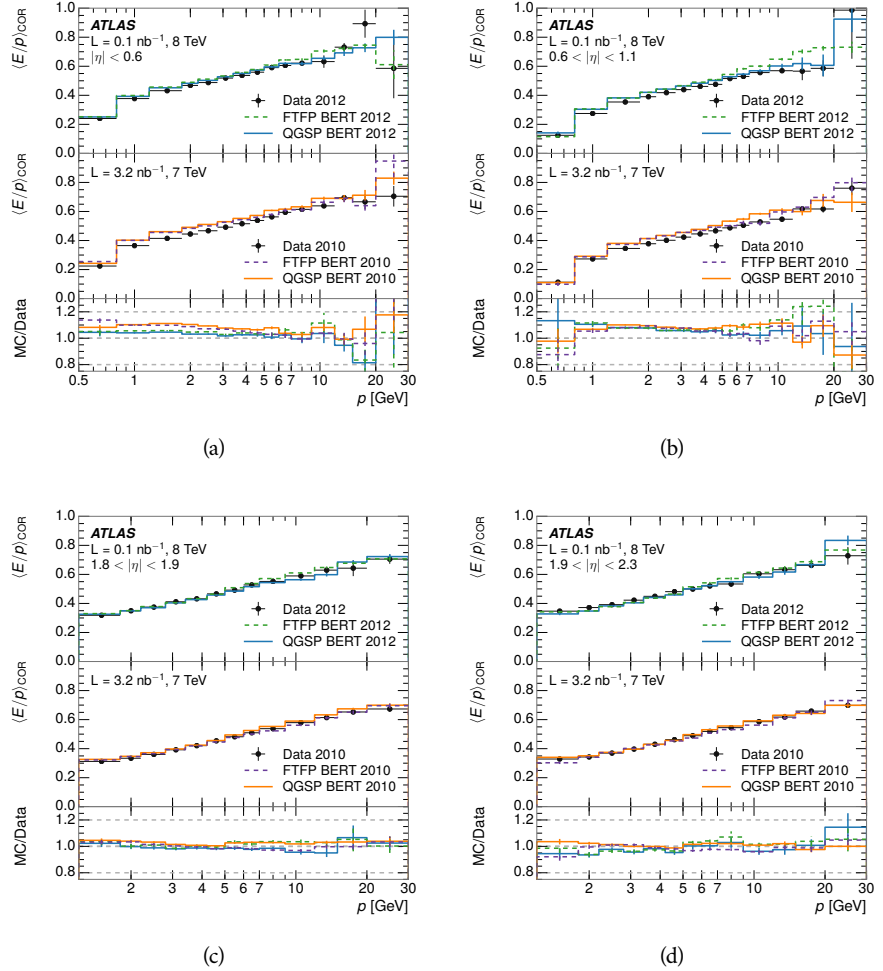


Figure 6: $\langle E/p \rangle_{\text{COR}}$ as a function of track momentum, for tracks with (a) $|\eta| < 0.6$, (b) $0.6 < |\eta| < 1.1$, (c) $1.8 < |\eta| < 1.9$, and (d) $1.9 < |\eta| < 2.3$.

577 ter weighted (LCW) energies, which accounts for those effects by calibrating the
 578 energy based on the properties of the cluster such as energy density and depth in
 579 the calorimeter. Figure 7 shows these distributions for tracks with zero or more
 580 clusters and separately for tracks with one or more clusters. The calibration
 581 moves $\langle E/p \rangle_{\text{COR}}$ significantly closer to 1.0, which is the purpose of the calibra-
 582 tion. The agreement between data and simulation improves noticeably when at
 583 least one cluster is required, as this removes the contribution from the mismod-
 584 eling of the zero fraction.

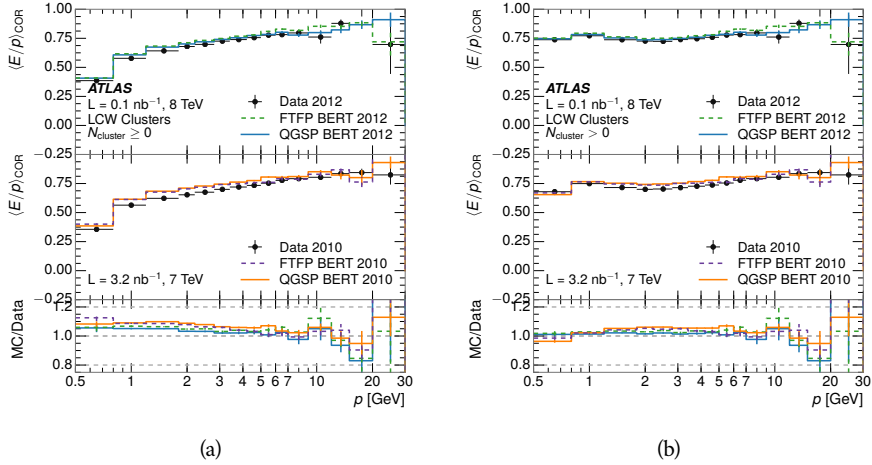


Figure 7: $\langle E/p \rangle_{\text{COR}}$ calculated using LCW-calibrated topological clusters as a function of track momentum for tracks with (a) zero or more associated topological clusters or (b) one or more associated topological clusters.

585 8.2.41 ADDITIONAL STUDIES

586 As has been seen in several previous measurements, the simulation does not
 587 correctly model the chance of a low momentum hadron to reach the calorime-
 588 ter. Because of the consistent discrepancy across pseudorapidity and interaction
 589 lengths, this seems to be best explained by incomplete understanding of hadronic
 590 interactions with the detector. For example, a hadron that scatters off of a nu-
 591 cleus in the inner detector can be deflected through a significant angle and not
 592 reach the expected location in the calorimeter. In addition, these interactions
 593 can produce secondary particles that are difficult to model.

594 The requirement on the number of hits in the TRT reduces these effects by
 595 preferentially selecting tracks that do not undergo nuclear interactions. It is inter-
 596 esting to check how well the simulation models tracks with low numbers of
 597 TRT hits, where the nuclear interactions are much more likely. Figure 8 com-
 598 pares the distributions with $N_{\text{TRT}} < 20$ to $N_{\text{TRT}} > 20$ for real and simulated
 599 particles. As expected, the tracks with fewer hits are poorly modeled in the sim-
 600 ulation as $\langle E/p \rangle_{\text{COR}}$ differs by as much as 25% at low momentum.

601 Another interesting aspect of the simulation is the description of antiprotons
 602 at low momentum, where QGSP_BERT and FTFP_BERT have significant differ-
 603 ences. This can be seen to have an effect in the inclusive response measurement

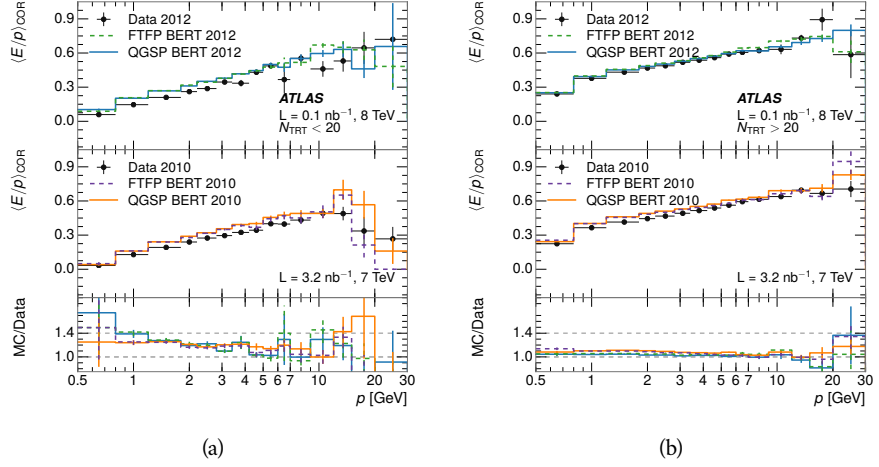


Figure 8: Comparison of the $\langle E/p \rangle_{\text{COR}}$ for tracks with (a) less than and (b) greater than 20 hits in the TRT.

when separated into positive and negative charge. The $\langle E/p \rangle_{\text{COR}}$ distributions for positive and negative particles are shown in Figure 9, where a small difference between QGSP_BERT and FTFP_BERT can be seen in the distribution for negative tracks. This is demonstrated more clearly in Figure 10, which shows the E/p distribution in the two simulations separated by charge. There is a clear difference around $E/p > 1.0$, which can be explained by the additional energy deposited by the annihilation of the antiproton in the calorimeter that is modeled well only in FTFP_BERT. This is also explored with data using identified antiprotons in Section 8.3.

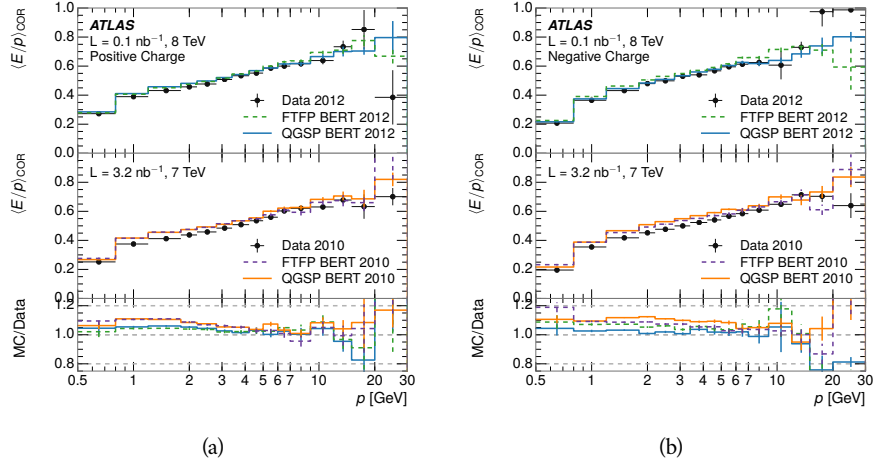


Figure 9: Comparison of the $\langle E/p \rangle_{\text{COR}}$ for (a) positive and (b) negative tracks as a function of track momentum for tracks with $|\eta| < 0.6$.

The $\langle E/p \rangle$ results in previous sections have considered the electromagnetic and hadronic calorimeters together as a single energy measurement, to emphasize the total energy deposited for a given particle. However, the deposits in each

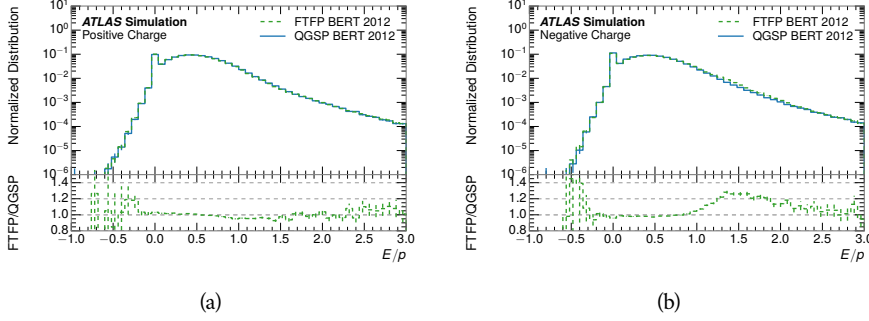


Figure 10: Comparison of the E/p distributions for (a) positive and (b) negative tracks with $0.8 < p/\text{GeV} < 1.2$ and $|\eta| < 0.6$, in simulation with the FTFP_BERT and QGSP_BERT physics lists.

calorimeter are available separately and $\langle E/p \rangle$ can be constructed for each layer. As the layers are composed of different materials and are modeled separately in the detector geometry, confirmation that the simulation matches the data well in each layer adds confidence in both the description of hadronic interactions with the two different materials and also the geometric description of each.

The technique discussed in Section 8.2.3 for selecting minimally ionizing particle (**MIP**s) in the electromagnetic calorimeter is also useful in studying deposits in the hadronic calorimeter. Those **MIP**s deposit almost all of their energy exclusively in the hadronic calorimeter. Figure 11 shows $\langle E/p \rangle_{\text{RAW}}^{\text{Had}}$, where RAW indicates that no correction has been applied for neutral backgrounds and Had indicates that only clusters for the hadronic calorimeter are included. The RAW and COR versions of $\langle E/p \rangle$ in this case are the same, as the neutral background is negligible in that calorimeter layer. The distributions are shown both for the original EM scale calibration and after LCW calibration. The data and simulation agree very well in this comparison, except in the lowest momentum bin which has 5% discrepancy that has already been seen in similar measurements.

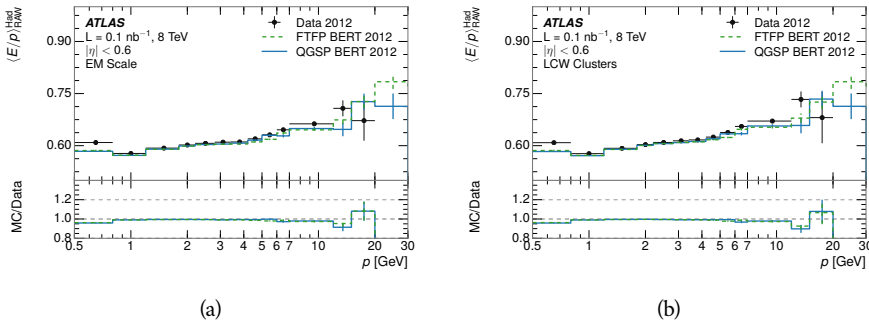


Figure 11: Comparison of the response of the hadronic calorimeter as a function of track momentum (a) at the EM-scale and (b) after the LCW calibration.

A similar comparison can be made in the electromagnetic calorimeter by selecting particles which have no associated energy in the hadronic calorimeter. These results are measured in terms of $\langle E/p \rangle_{\text{COR}}^{\text{EM}}$, where EM designates that

only clusters in the electromagnetic calorimeter are included and COR designates that the neutral background is subtracted as the neutral background is present in this case. Figure 12 shows the analogous comparisons to Figure 11 in the electromagnetic calorimeter. In this case the disagreement between data and simulation is more pronounced, with discrepancies as high as 5% over a larger range of momenta. This level of discrepancy indicates that the description of the electromagnetic calorimeter is actually the dominant source of discrepancy in the combined distributions in Section 8.2.4.

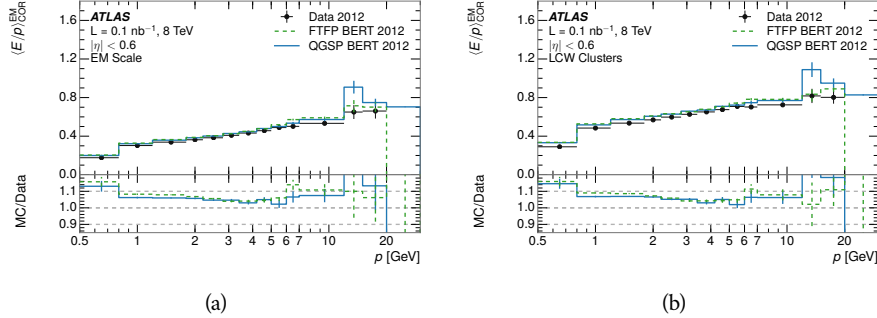


Figure 12: Comparison of the response of the EM calorimeter as a function of track momentum (a) at the EM-scale and (b) with the LCW calibration.

NOTE: There are more studies that I skipped for brevity that could be included if interesting. E/p at different cluster threshold settings, E/p with pileup, E/p with cells. I also left out a lot of eta bins that appear in the paper so that this section didn't turn into 20 pages of plots.

8.3 IDENTIFIED PARTICLE RESPONSE

The inclusive response measurement for hadrons can be augmented by measuring the response for specific particle species. The simulation models each particle type separately, and understanding the properties of each is important in constraining the uncertainty on jets. In order to select and measure specific hadrons, this section relies on the displaced decays of long-lived particles. Such decays can be identified by reconstructing secondary vertices with a requirement on mass. In particular, Λ , $\bar{\Lambda}$, and K_S^0 can be used to select a pure sample of protons, antiprotons, and pions, respectively.

8.3.1 DECAY RECONSTRUCTION

The measurement of response for identified particles uses the same selection as for inclusive particles (Section 8.1.3) with a few additions. Each event used is required to have at least one secondary vertex, and the tracks are required to match to that vertex rather than the primary vertex. Pions are selected from decays of $K_S^0 \rightarrow \pi^+ \pi^-$, which is the dominant decay for K_S^0 to charged particles. Protons are selected from decays of $\Lambda \rightarrow \pi^- p$ and antiprotons from $\bar{\Lambda} \rightarrow \pi^+ \bar{p}$,

which are similarly the dominant decays of Λ and $\bar{\Lambda}$ to charged particles. The species of parent hadron in these decays is determined by reconstructing the mass of the tracks associated to the secondary vertex. The sign of the higher momentum decay particle can distinguish between Λ and $\bar{\Lambda}$, which of course have the same mass, as the proton or antiproton is kinematically favored to have higher momentum. Examples of the reconstructed masses used to select these decays are shown in Figure 13.

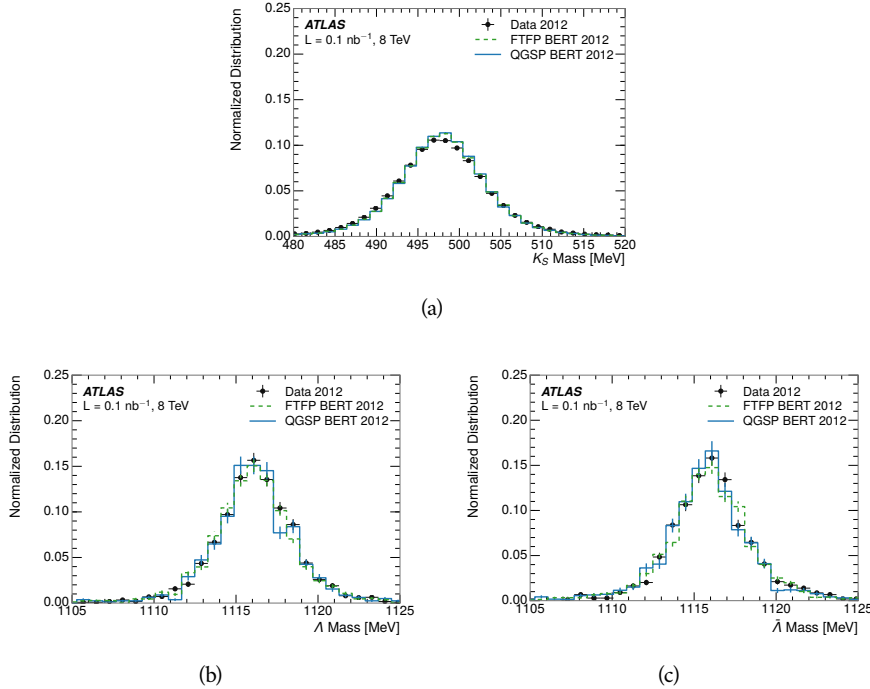


Figure 13: The reconstructed mass peaks of (a) K_S^0 , (b) Λ , and (c) $\bar{\Lambda}$ candidates.

The dominant backgrounds for the identified particle decays are nuclear interactions and combinatoric sources. These are suppressed by the kinematic requirements on the tracks as well as an additional veto which removes candidates that are consistent with both a Λ or $\bar{\Lambda}$ and a K_S^0 hypothesis, which is possible because of the different assumptions on particle mass in each case [5]. After these requirements, the backgrounds are found to be negligible compared to the statistical errors on these measurements.

8.3.2 IDENTIFIED RESPONSE

With these techniques the E/p distributions are extracted in data and simulation for each particle species and shown in Figure 14. These distributions are shown for a particular bin of E_a ($2.2 < E_a/\text{GeV} < 2.8$), rather than p . E_a is the energy available to be deposited in the calorimeter: for pions $E_a = \sqrt{p^2 + m^2}$, for protons $E_a = \sqrt{p^2 + m^2} - m$, and for antiprotons $E_a = \sqrt{p^2 + m^2} + m$. The features of the E/p distributions are similar to the inclusive case. There is a small negative tail from noise and a large fraction of tracks with zero energy from particles which do not reach the calorimeter. The long positive tail is noticeably more

686 pronounced for antiprotons because of the additional energy generated by the
 687 annihilation in addition to the neutral background.

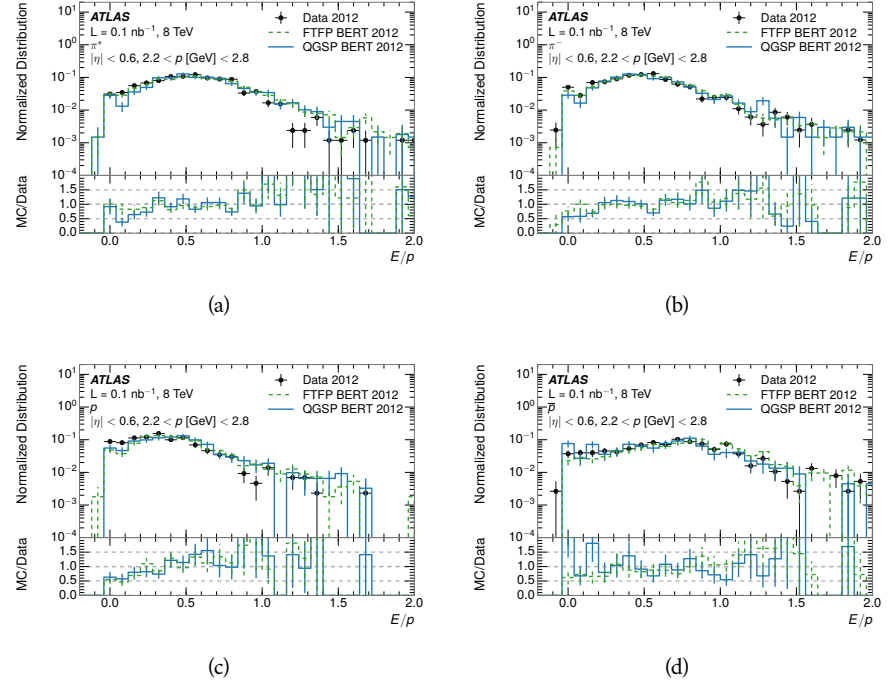


Figure 14: The E/p distribution for isolated (a) π^+ , (b) π^- , (c) proton, and (d) anti-proton tracks.

688 The zero fraction is further explored in Figure 15 for pions and protons in data
 689 and simulation. The simulation consistently underestimates the zero fraction
 690 independent of particle species, which implies that this discrepancy is not caused
 691 by the model of a particular species but rather a feature common to all.

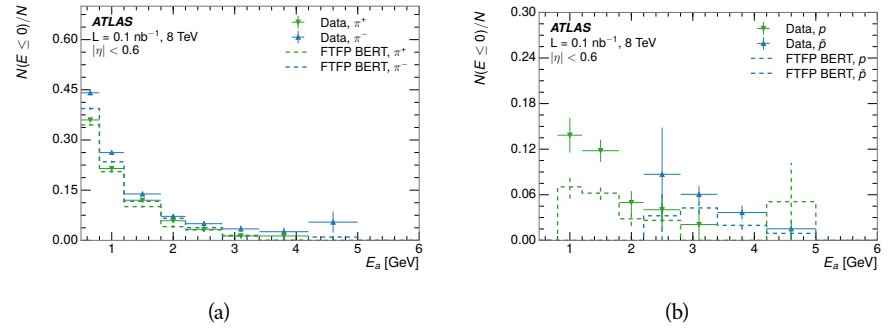


Figure 15: The fraction of tracks with $E \leq 0$ for identified (a) π^+ and π^- , and (b) proton and anti-proton tracks

692 It is also interesting to compare the response between the different particle
 693 species. One approach to do this is to measure the difference in $\langle E/p \rangle$ between
 694 two types, which has the advantage of removing the neutral background. These
 695 differences are shown in various combinations in Figure 16. The response for

π^+ is greater on average than the response to π^- because of a charge-exchange effect which causes the production of additional neutral pions in the showers of π^+ [27]. The response for π^+ is also greater on average than the response to p , because a large fraction of the energy of π^+ hadrons is converted to an electromagnetic shower [28, 29]. However, the \bar{p} response is significantly higher than the response to π^- because of the annihilation of the antiproton. FTFP_BERT does a better job of modeling this effect than QGSP_BERT because of their different descriptions of \bar{p} interactions with material.

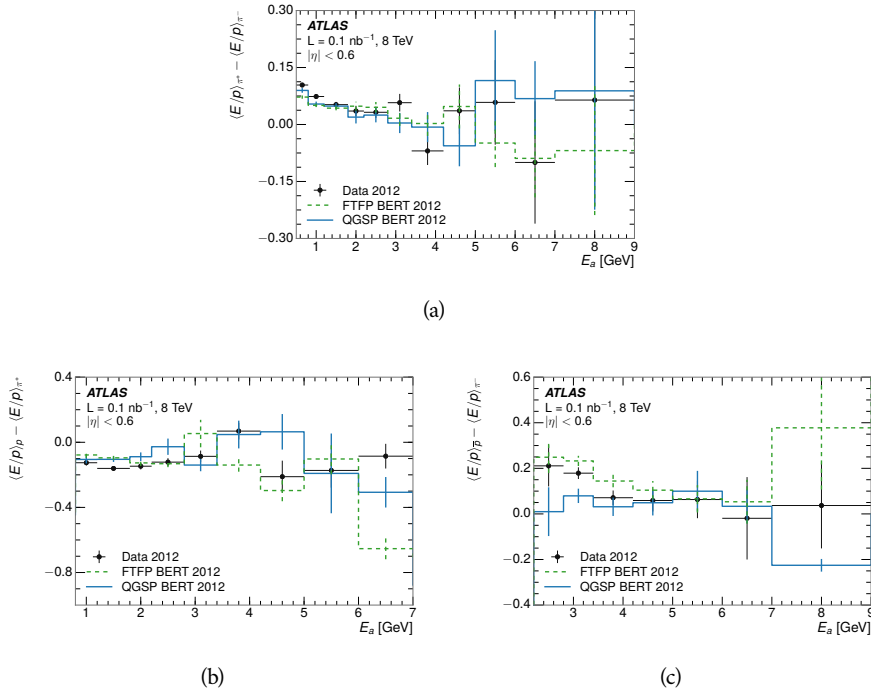


Figure 16: The difference in $\langle E/p \rangle$ between (a) π^+ and π^- (b) p and π^+ , and (c) \bar{p} and π^- .

It is also possible to remove the neutral background from these response distributions using the same technique as in Section 8.2.3. The technique is largely independent of the particle species and so can be directly applied to $\langle E/p \rangle$ for pions. The $\langle E/p \rangle_{\text{COR}}$ distributions for pions are shown in Figure 17, which are very similar to the inclusive results. The inclusive hadrons are comprised mostly of pions, so this similarity is not surprising. It is also possible to see the small differences between π^+ and π^- response here, where $\langle E/p \rangle_{\text{COR}}$ is higher on average for π^+ . The agreement between data and simulation is significantly worse for the π^- distributions than for the π^+ , with a discrepancy greater than 10% below 2-3 GeV.

8.3.3 ADDITIONAL SPECIES IN SIMULATION

The techniques above provide a method to measure the response separately for only pions and protons. However the hadrons which forms jets include a number of additional species such as kaons and neutrons. The charged kaons are

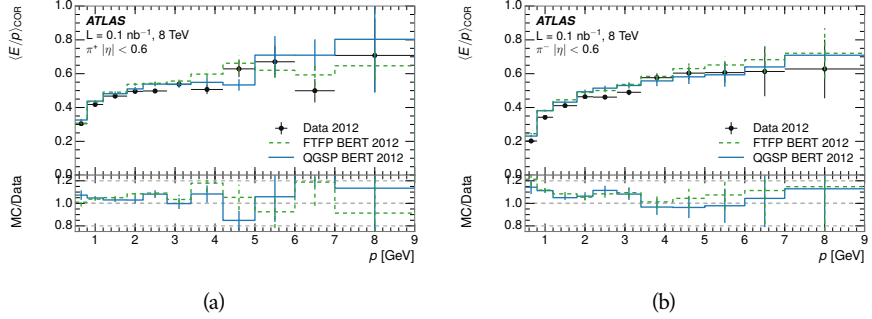


Figure 17: $\langle E/p \rangle_{\text{COR}}$ as a function of track momentum for (a) π^+ tracks and (b) π^- tracks.

an important component of the inclusive charged hadron distribution, which is comprised of roughly 60-70% pions, 15-20% kaons, and 5-15% protons. These are difficult to measure in data at the ATLAS detector, although a template subtraction technique has been proposed which may be effective with larger sample sizes [4]. The simulation of these particles includes noticeable differences in response at low energies, which are shown in Figure 18 for FTFP_BERT. The significant differences in response between low energy protons and antiprotons are accounted for above in the definitions of E_a .

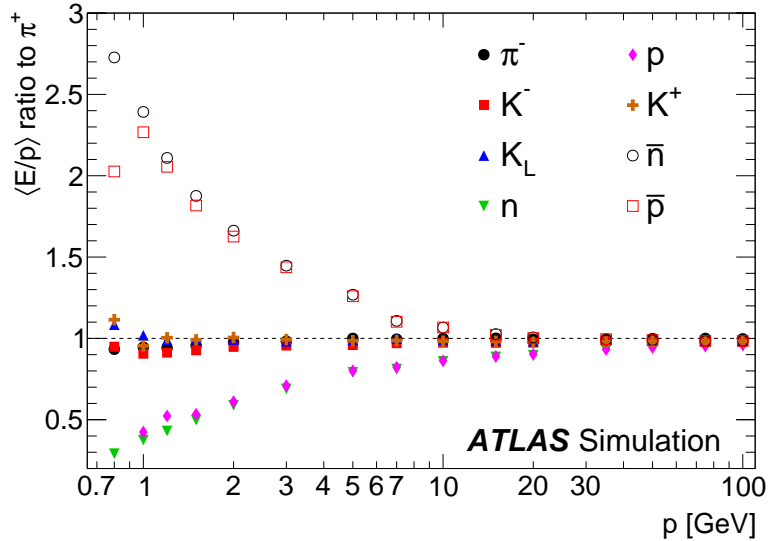


Figure 18: The ratio of the calorimeter response to single particles of various species to the calorimeter response to π^+ with the physics list FTFP_BERT.

8.4 SUMMARY

These various measurements of calorimeter response shown above for data and simulation illuminate the accuracy of the simulation of hadronic interactions at the ATLAS detector. The results were done using 2010 and 2012 data at 7 and 8

730 TeV, but reflect the most current understanding of the detector alignment and
731 geometry. A number of measurements focusing on a comparison between pro-
732 tons and antiprotons suggest that FTFP_BERT models those interaction more
733 accurately than QGSP_BERT. These measurements, among others, were the moti-
734 vation to switch the default Geant4 simulation from FTFP_BERT to QGSP_BERT
735 for all ATLAS samples.

736 Even with these updates, there are a number of small, approximately 5%, dis-
737 crepancies in response between the data and simulation at low energies. At
738 higher energies the simulation of hadronic interactions is very consistent with
739 data. Chapter 9 discusses how to use these observed differences to constrain the
740 jet energy scale and its associated uncertainties.

741

742 JET ENERGY RESPONSE AND UNCERTAINTY

743 9.1 MOTIVATION

744 As jets form a major component of many physics analyses at ATLAS, it is cru-
 745 cial to carefully calibrate the measurement of jet energies and to derive an un-
 746 certainty on that measurement. These uncertainties have often been the dom-
 747 inant systematic uncertainty in high-energy analyses at the Large Hadron Col-
 748 llider ([LHC](#)). Dijet and multijet balance techniques provide a method to constrain
 749 the [JES](#) and its uncertainty in data, and provide the default values used for ATLAS
 750 jet measurements at most energies [30]. These techniques are limited by their re-
 751 liance on measuring jets in data, so they are statistically limited in estimating
 752 the jet energy scale at the highest jet energies. This chapter presents another
 753 method for estimating the jet energy scale and its uncertainty which builds up a
 754 jet from its components and thus can be naturally extended to high jet momen-
 755 tum. Throughout this chapter the jets studied are simulated using [Pythia8](#) with
 756 the CT10 parton distribution set [31] and the AU2 tune [8], and corrections are
 757 taken from the studies including data and simulation in Chapter 8.

758 As described in Section 7.2, jets are formed from topological clusters of energy
 759 in the calorimeters using the anti- k_t algorithm. These clusters originate from a
 760 diverse spectrum of particles, in terms of both species and momentum, leading to
 761 significantly varied jet properties and response between jets of similar produced
 762 momentum. Figure 19 shows the simulated distribution of particles within jets
 763 at a few examples energies. The E/p measurements provide a thorough under-
 764 standing of the dominant particle content of jets, the charged hadrons.

765 9.2 UNCERTAINTY ESTIMATE

766 Simulated jets are not necessarily expected to correctly model the energy de-
 767 posits in the calorimeters, because of the various discrepancies discussed in Chap-
 768 ter 8. To evaluate a jet energy response, the simulated jet energies are compared
 769 to a corrected jet built up at the particle level. Each cluster in a jet is associated
 770 to the truth particle which deposited it, and the energy in that cluster is then
 771 corrected for a number of effects based on measurements in data. The primary
 772 corrections come from the single hadron response measurements in addition
 773 to response measured using the combined test beam which covers higher mo-
 774 mentum particles [32]. These corrections include both a shift (Δ), in order to
 775 make the simulation match the average response in data, and an uncertainty (σ)
 776 associated with the ability to constrain the difference between data and simula-
 777 tion. Some of the dominant sources of uncertainty are itemized in Table 1 with
 778 typical values, and the full list considered is described in detail in the associated

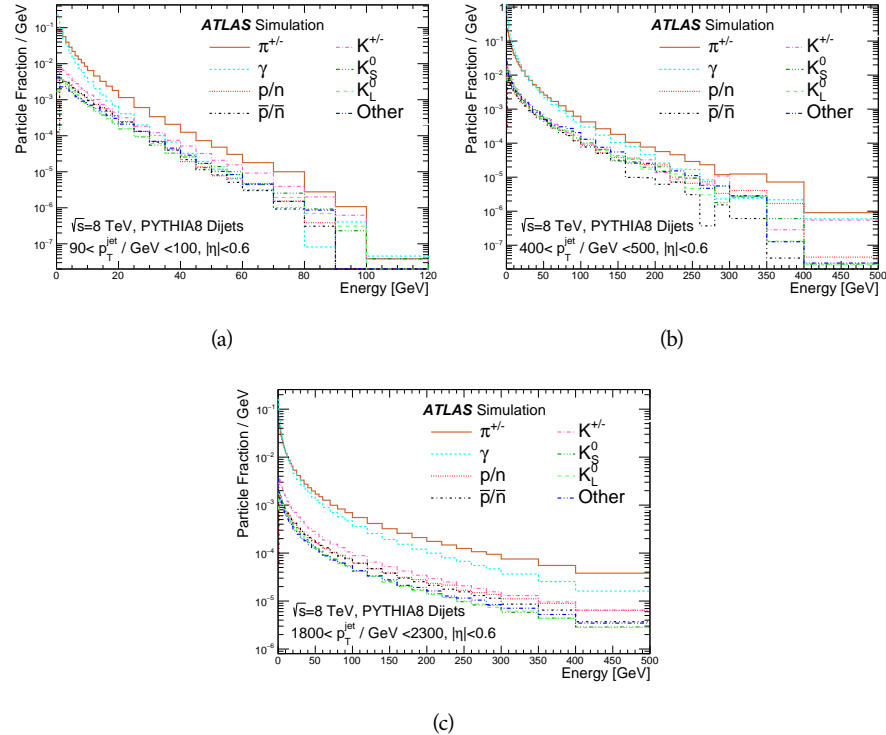


Figure 19: The spectra of true particles inside anti- k_t , $R = 0.4$ jets with (a) $90 < p_T/\text{GeV} < 100$, (b) $400 < p_T/\text{GeV} < 500$, and (c) $1800 < p_T/\text{GeV} < 2300$.

paper [4]. These uncertainties cover differences between the data and simulation in the modeling of calorimeter response to a given particle. No uncertainties are added for the difference between particle composition of jets in data and simulation.

From these terms, the jet energy scale and uncertainty is built up from individual energy deposits in simulation. Each uncertainty term is treated independently, and are taken to be gaussian distributed. The resulting scale and uncertainty is shown in Figure 20, where the mean response is measured relative to the calibrated energy reported by simulation. The dominant uncertainties come from the statistical uncertainties on the E/p measurements at lower energies and the additional uncertainty for out of range measurements at higher energies. The total uncertainty from this method at intermediate jet energies is comparable to other simulation-based methods [33] and is about twice as large as in-situ methods using data [30]. This method is the only one which provides an estimation above 1.8 TeV, however, and so is still a crucial technique in analyses that search for very energetic jets.

These techniques can also be used to measure the correlation between bins of average reconstructed jet momentum across a range of p_T and $|\eta|$, where correlations are expected because of a similarity in particle composition at similar energies. Figure 21 shows these correlations, where the uncertainties on jets in neighboring bins are typically between 30% and 60% correlated. The uncertainty on all jets becomes significantly correlated at high energies and larger pseudora-

Abbrev.	Description	Δ (%)	σ (%)
In situ E/p	The comparison of $\langle E/p \rangle_{\text{COR}}$ as described in Chapter 8 with statistical uncertainties from 500 MeV to 20 GeV.	0-3	1-5
CTB	The main $\langle E/p \rangle$ comparison uncertainties, binned in p and $ \eta $, as derived from the combined test beam results, from 20 to 350 GeV [32].	0-3	1-5
E/p Zero Fraction	The difference in the zero-fraction between data and MC simulation from 500 MeV to 20 GeV.	5-25	1-5
E/p Threshold	The uncertainty in the EM calorimeter response from the potential mismodeling of threshold effects in topological clustering.	0	0-10
Neutral	The uncertainty in the calorimeter response to neutral hadrons based on studies of physics model variations.	0	5-10
K_L	An additional uncertainty in the response to neutral K_L in the calorimeter based on studies of physics model variations.	0	20
E/p Misalignment	The uncertainty in the p measurement from misalignment of the ID.	0	1
Hadrons, $p > 350$ GeV	A flat uncertainty for all particles above the energy range or outside the longitudinal range probed with the combined test beam.	0	10

Table 1: The dominant sources of corrections and systematic uncertainties in the [JES](#) estimation technique, including typical values for the correcting shift (Δ) and the associated uncertainty (σ).

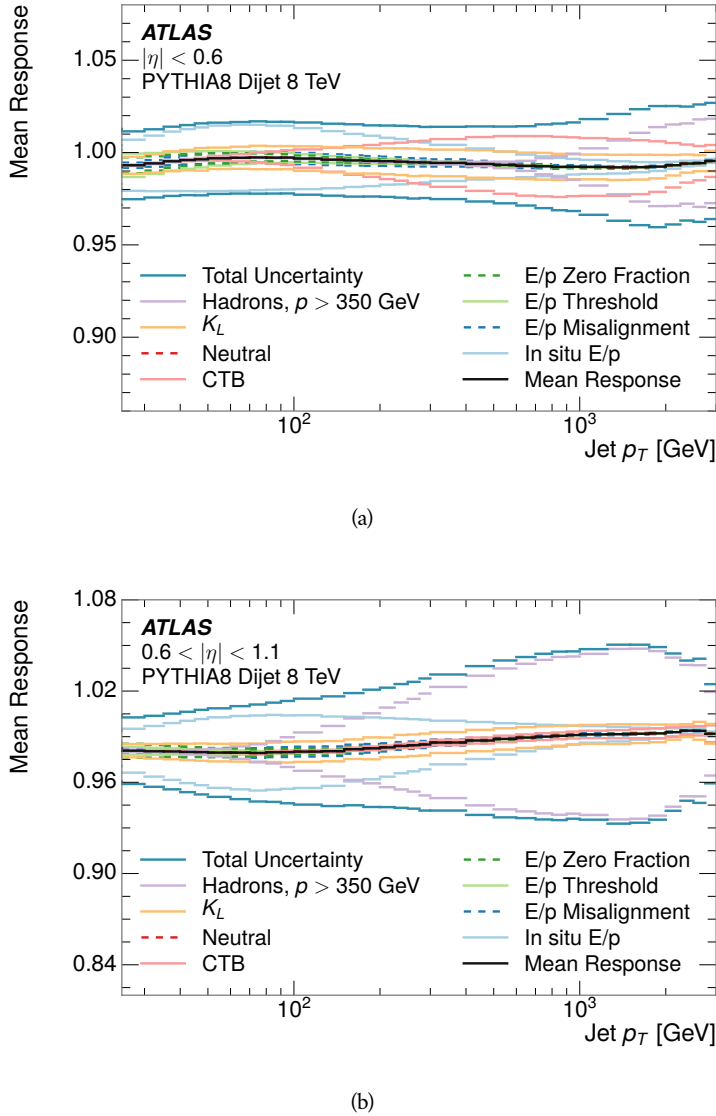


Figure 20: The [JES](#) uncertainty contributions, as well as the total [JES](#) uncertainty, as a function of jet p_T for (a) $|\eta| < 0.6$ and (b) $0.6 < |\eta| < 1.1$.

801 pidities, when the uncertainty becomes dominated by the single term reflecting
 802 out of range particles.

803 9.3 SUMMARY

804 The technique described above provides a jet energy scale and uncertainty by
 805 building up jet corrections from the energy deposits of constituent particles. The
 806 E/p measurements are crucial in providing corrections for the majority of parti-
 807 cles in the jets. The uncertainty derived this way is between 2 and 5% and is about
 808 twice as large at corresponding momentum than jet balance methods. However
 809 this is the only uncertainty available for very energetic jets using 2012 data and
 810 simulation, and repeating this method with Run 2 data and simulation will be

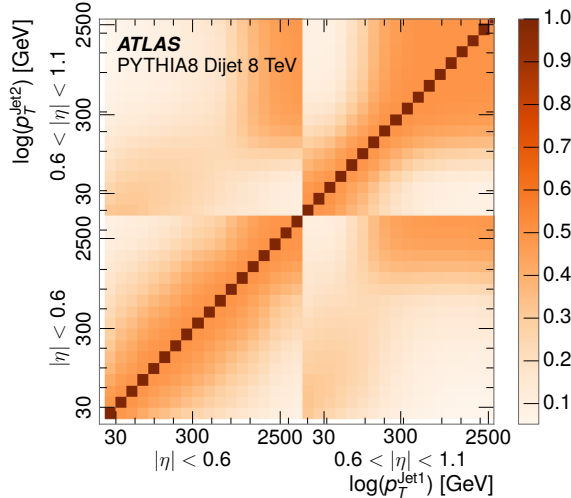


Figure 21: The JES correlations as a function of jet p_T and $|\eta|$ for jets in the central region of the detector.

811 important in providing an uncertainty for the most energetic jets in 13 TeV col-
 812 lisions.

813

PART V

814

SEARCH FOR LONG-LIVED PARTICLES

815

You can put some informational part preamble text here.

10

816

817 LONG-LIVED PARTICLES IN ATLAS

818 10.1 OVERVIEW AND CHARACTERISTICS

819 10.2 SIMULATION

820

821 EVENT SELECTION

822 The Long-Lived Particles ([LLPs](#)) targeted by this search differ in their interactions
 823 with the detector from [SM](#) particles primarily because of their large mass. When
 824 produced at the energies available at the [LHC](#), that large mass results in a low β .
 825 Such slow-moving particles heavily ionize in detector material. Each layer of
 826 the pixel detector provides a measurement of that ionization, through time over
 827 threshold ([ToT](#)), as discussed in Section [6.3.1](#). The ionization in the pixel detector,
 828 quantified in terms of dE/dx , provides the major focus for this search technique.
 829 It is effective both for its discriminating power and also because of the large range
 830 of lifetimes where it can be used. However dE/dx needs to be augmented with
 831 a few additional selection requirements to form a complete search.

832 Ionization is not currently available in any form during triggering, so this
 833 search instead relies on E_T^{miss} to trigger signal events. Although triggering on
 834 E_T^{miss} can be inefficient, E_T^{miss} is often large for many production mechanisms
 835 of [LLPs](#), as discussed in Section [10.1](#).

836 Ionization is most effective in rejecting backgrounds for well-measured, high-
 837 momentum tracks, so some basic requirements on quality and kinematics are
 838 placed on the particles considered in this search. In particular a newly intro-
 839 duced tracking variable is very effective in removing highly-ionizing backgrounds
 840 caused by overlapping tracks. A few additional requirements are placed on the
 841 tracks considered for [LLP](#) candidates that increase background rejection by tar-
 842 geting specific types of [SM](#) particles. These techniques provide a significant anal-
 843 ysis improvement over previous iterations of ionization-based searches on AT-
 844 LAS by providing additional background rejection with minimal loss in signal
 845 efficiency.

846 The ionization measurement with the Pixel detector can be calibrated to pro-
 847 vide an estimator of $\beta\gamma$. That estimate, together with the momentum measure-
 848 ment provided by tracking, can be used to reconstruct a mass for each track
 849 which traverses the pixel detector. That mass variable will be peaked at the [LLP](#)
 850 mass for any signal, and provides an additional tool to search for an excess. In
 851 addition to an explicit requirement on ionization, this search constructs a mass-
 852 window for each targeted signal mass in order to evaluate any excess of events
 853 and to set limits.

854 The strategy discussed here is optimized for lifetimes of $O(1)$ - $O(10)$ ns.
 855 Pixel ionization is especially useful in this regime as particles only need to prop-
 856 agate through the first seven layers of the inner detector, about 37 cm from the
 857 beam axis. The search is still competitive with other searches for [LLPs](#) at longer
 858 lifetimes, because the primary discriminating variables are still applicable even
 859 for particles that do not decay within the detector [34]. Although the basic strat-
 860 egy remains the same for all lifetimes, two signal regions are defined to optimize
 861 separately for intermediate and long lifetime particles.

862 11.1 TRIGGER

863 Triggering remains a significant difficulty in defining an event selection with
 864 high signal efficiency in a search for [LLPs](#). There are no triggers available in
 865 the current ATLAS system that can fire directly from a high momentum track
 866 with large ionization (Section 6.6). Although in some configurations a charged
 867 [LLP](#) can fire muon triggers, this requirement introduces significant model depen-
 868 dence on both the allowed lifetimes and the interactions in the calorimeter [35].

869 For a search targeting particles which may decay prior to reaching the muon
 870 system, the most efficient available trigger is based on missing energy [35]. As
 871 discussed in Section 10.1, signal events can produce E_T^{miss} by two primary mech-
 872 anisms. The decays of R-Hadrons to neutralinos can produce missing energy
 873 when the neutralinos go undetected in the calorimeters. [LLPs](#) which do not de-
 874 cay before the calorimeters also can produce missing energy because they do not
 875 deposit much energy. Either case to some extent relies on kinematic degrees of
 876 freedom to produce missing energy, as the pair-produced [LLPs](#) tend to balance
 877 each other in the transverse plain. That balance results in a relatively low ef-
 878 ficiency for long-lifetime particles, roughly 40%, and efficiencies between 65%
 879 and 95% for shorter lifetimes depending on both the mass and the lifetime.

880 11.2 KINEMATICS AND ISOLATION

881 After the trigger requirement, each event is required to have a primary vertex
 882 reconstructed from at least two well-measured tracks in the inner detector, each
 883 with $p_T > 400$ MeV. If more than one such vertex exists, the primary vertex
 884 is taken to be the one with the largest summed track momentum for all tracks
 885 associated to that vertex. The offline reconstructed E_T^{miss} is required to be above
 886 130 GeV to additionally reject [SM](#) backgrounds. The transverse missing energy
 887 is calculated using fully reconstructed and calibrated offline objects, as described
 888 in Section 7.5. In particular the E_T^{miss} definition in this selection uses jets recon-
 889 structed with the anti- k_t algorithm with radius $R = 0.4$ from clusters of energy
 890 in the calorimeter (Section 7.2) and with $p_T > 20$ GeV, as well as reconstructed
 891 muons, electrons, and tracks not identified as another object type.

892 The E_T^{miss} distributions are shown for data and a few simulated signals in Fig-
 893 ure 22, after the trigger requirement. The cut placed at 130 GeV is 95% effi-
 894 cient for metastable and 90% efficient for stable particles, because of the missing
 895 energy generating mechanisms discussed previously. The distribution of data
 896 in this figure and subsequent figures in this section can be interpreted as the
 897 distribution of backgrounds, as any signal contamination would be negligible if
 898 present at these early stages of the selection (prior to the final requirement on
 899 ionization). The background falls rapidly with missing energy, motivating the
 900 direct requirement on E_T^{miss} for the signal region. Although a tighter require-
 901 ment than the specified value of 130 GeV would seem to increase the search
 902 potential from these early distributions, other requirements are more optimal
 903 when taken as a whole. The specific values for each requirement in signal region
 904 were optimized considering the increase in discovery reach for tightening the

requirement on each discriminating variable. **NOTE: Is it interesting to discuss the signal region optimization process in detail? I could add another section on how the values were determined, although in truth it is at least partially historical precedence.**

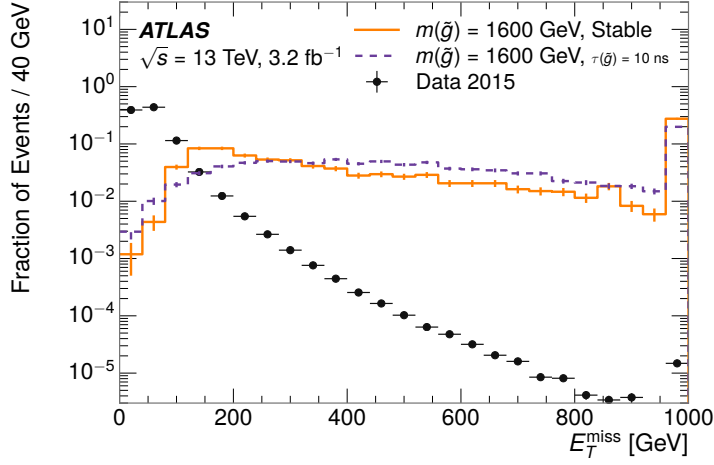


Figure 22: The distribution of E_T^{miss} for data and simulated signal events, after the trigger requirement.

Potential signal events are then required to have at least one candidate LLP track. Although the LLPs are produced in pairs, many models do not consistently yield two charged particles. For example, in the R-Hadron model highlighted here, only 20% of events have two charged R-Hadrons while 47% of events have just one. A signal region requiring two charged candidates could be a powerful improvement in background rejection for a larger dataset, but it is not considered in this version of the analysis as it was found to be unnecessary to reject the majority of backgrounds.

For a track to be selected as a candidate, it must have $p_T > 50 \text{ GeV}$ and pass basic quality requirements. The track must be associated to the primary vertex. It must also have at least seven clusters in the silicon layers in the inner detector to ensure an accurate measurement of momentum. Those clusters must include one in the innermost layer if the extrapolated track is expected to pass through that layer. And to ensure a reliable measurement of ionization, the track is required to have at least two clusters in the pixel detector that provide a measurement of dE/dx .

At this point in the selection, there is a significant high-ionization background from multiple tracks that significantly overlap in the inner detector. Previous version of this analysis have rejected these overlaps by an explicit overlap rejection between pairs of fully reconstructed tracks, typically by requiring no additional tracks within a cone around the candidate. This technique, however, fails to remove the background from tracks that overlap so precisely that the tracks cannot be separately resolved.

A new method, added in Run 2, identifies cluster shapes that are likely formed by multiple tracks based on a neural network classification algorithm. The num-

934 ber of clusters that are classified this way in the pixel detector for a given track
 935 is called N_{split} . As the shape of clusters requires significantly less spatial sepa-
 936 ration to identify overlaps than it does to reconstruct two fully resolved tracks,
 937 this variable is more effective at rejecting backgrounds from overlaps. Figure 23
 938 shows the dependence of ionization on N_{split} ; as N_{split} increases the most prob-
 939 able value of dE/dx grows significantly up to twice the expected value when
 940 $N_{\text{split}} = 4$.

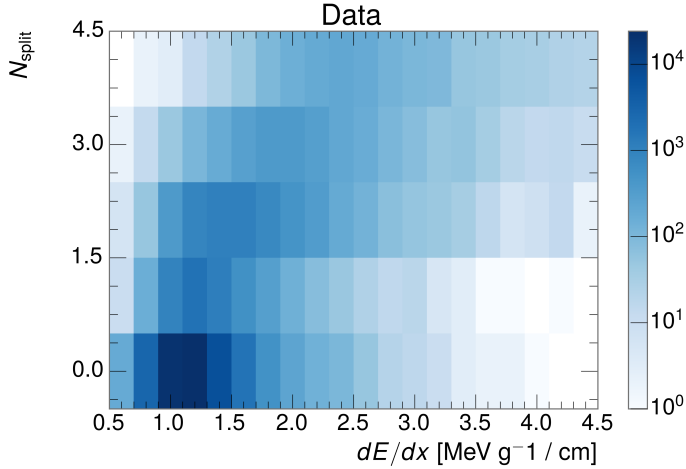


Figure 23: The dependence of dE/dx on N_{split} in data after basic track hit requirements have been applied.

941 This requirement is very successful in reducing the long positive tail of the
 942 dE/dx distributions, as can be seen in Figure 24. Comparing the distribution for
 943 “baseline tracks”, tracks with only the above requirements on clusters applied and
 944 before the requirement on N_{split} , to the distribution with $N_{\text{split}} = 0$, it is clear
 945 that the fraction of tracks with large dE/dx is reduced by several orders of mag-
 946 nitude. The isolated tracks are very close to the dE/dx distribution of identified
 947 muons, which are extremely well isolated on average. Figure 24 also includes
 948 the distribution of dE/dx in an example signal simulation to demonstrate how
 949 effective dE/dx is as a discriminating variable with this isolation applied. The
 950 background falls rapidly for $dE/dx > 1.8 \text{ MeVg}^{-1}\text{cm}^2$ while the majority of
 951 the signal, approximately 90% depending on the mass, falls above that threshold.
 952 Over 90% of **LLP** tracks in simulated signal events pass the N_{split} -based isolation
 953 requirement.

954 A few additional kinematic requirements are imposed to help reduce **SM** back-
 955 grounds. The momentum of the candidate track must be at least 150 GeV, and
 956 the uncertainty on that measurement must be less than 50%. The distribution of
 957 momentum is shown in Figure 25 for tracks in data and simulated signal events
 958 after the previously discussed requirements on clusters, transverse momentum,
 959 and isolation have been imposed. The signal particles are much harder on aver-

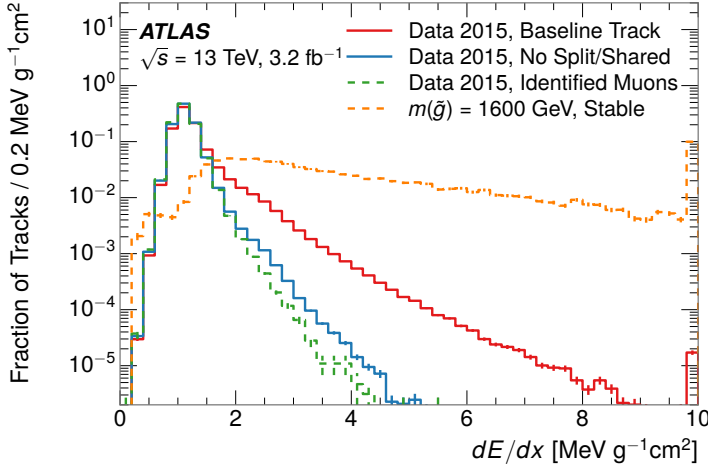


Figure 24: The distribution of dE/dx with various selections applied in data and simulated events.

age than their backgrounds because of the high energy interactions required to produce them. The transverse mass, M_T , defined as

$$M_T = \sqrt{2p_T E_T^{\text{miss}}(1 - \cos(\Delta\phi(E_T^{\text{miss}}, \text{track})))} \quad (1)$$

estimates the mass of a decay of to a single charged particle and an undetected particle and is required to be greater than 130 GeV to reject contributions from the decay of W bosons. Figure 26 shows the distribution of M_T for data and simulated signal events. The signal is distributed over a wide range of M_T , with about 90% above the threshold value of 130 GeV. The data shows a dual-peaked structure, where the first peak comes from W boson decays and the second peak is a kinematic shaping from the requirements on E_T^{miss} and the track p_T in dijet events.

11.3 STANDARD MODEL REJECTION

Because this search selects events with just a single, highly-ionizing track, backgrounds can be formed by a wide variety of SM processes when various charged particles have a few randomly large deposits of energy in the pixel detector. Those backgrounds can be effectively rejected by targeting the types of particles produced rather than the processes which produce them, as LLPs will have significant differences compared to any SM particle. These rejections focus on using additional features of the event, other than the kinematics or ionization of the candidate track, as they can provide a powerful source of background rejection with very high signal efficiency. The lifetime of the particle can significantly change its detector characteristics, as discussed in Section 10.1. To accommodate these differences, the SM rejections defined in this section are split to form two signal regions, one for long-lifetimes particles, the “stable” region, and one for intermediate lifetime particles, the “metastable” region.

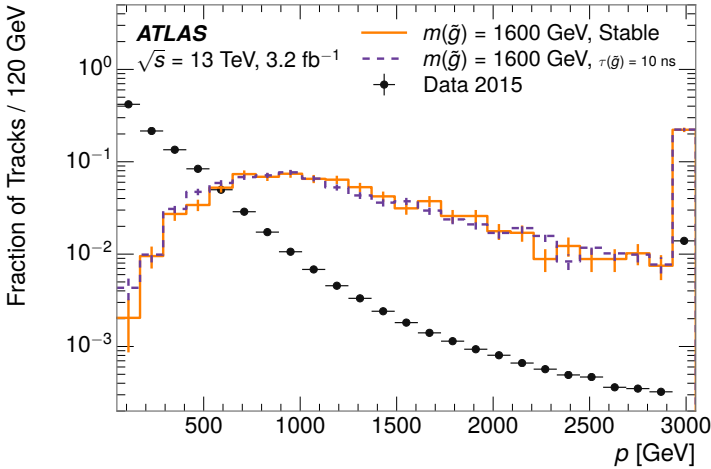


Figure 25: The distribution of track momentum for data and simulated signal events, after previous selection requirements have been applied.

984 Jets can be very effectively rejected by considering the larger-scale isolation of
 985 the candidate track. In this case the isolation focuses on the production of nearby
 986 particles as a jet-veto, rather than isolation from overlapping tracks to reduce
 987 high-ionization backgrounds. As explained in Section 10.1, the fragmentation
 988 process which produces an R-Hadron is very hard and thus is not expected to
 989 produce additional particles. The jet-veto uses the summed momentum of tracks
 990 with a cone of $\Delta R < 0.25$, referred to as p_T^{Cone} , which is shown in Figure 27 for
 991 data and simulated signal events. In the data this value has a peak at zero from
 992 isolated tracks such as leptons, and a long tail from jets which contains as much
 993 as 80% of the background above 20 GeV at this stage of the selection. In signal
 994 events p_T^{Cone} is strongly peaked at zero and significantly less than 1% is above 20
 995 GeV. This makes a requirement of $p_T^{\text{Cone}} < 20$ GeV one of the most effective
 996 methods to reject background without losing signal efficiency. For the stable
 997 signal region, this cut is further tightened to $p_T^{\text{Cone}} < 5$ GeV as it is the most
 998 effective variable remaining to extend the search reach for long lifetimes.

999 Even for fully isolated particles, there are additional methods to reject each
 1000 type of particle using information in the muon system and calorimeters. Muons
 1001 can be identified very reliably using the tracks in the muon system, as described
 1002 in Section 7.4. For intermediate lifetimes the LLPs do not survive long enough
 1003 to reach the muon system, and so muons are vetoed by rejecting tracks that as-
 1004 sociate to a muon with medium muon identification requirements. For longer
 1005 lifetimes, this rejection is not applied because LLPs which reach the muon system
 1006 can be identified as muons as often as 30% of the time in simulated samples.

1007 Calorimeter-based particle rejection relies on the expected small deposits of
 1008 energy from LLPs. When the lifetime is long enough to reach the calorimeter, a
 1009 LLP deposits little of its energy as it traverses the material, as discussed in Sec-
 1010 tion 10.1. Even when the particle does decay before the calorimeter, the major-
 1011 ity of its energy is carried away by the Lightest Supersymmetric Particle (LSP)
 1012 and not deposited in the calorimeter. In both cases the energy is expected to be

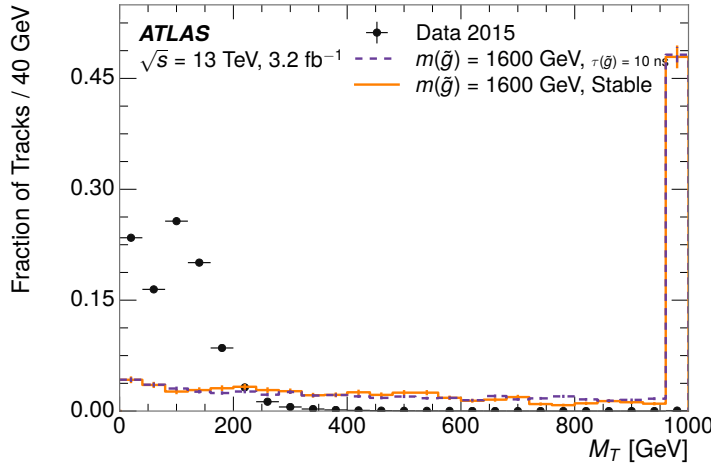


Figure 26: The distribution of M_T for data and simulated signal events, after previous selection requirements have been applied.

1013 distributed across the layers of the calorimeters and not peaked in just one layer.
 1014 This can be quantified in terms of E/p , the ratio of calorimeter energy of a nearby
 1015 jet to the track momentum, and f_{EM} , the fraction of energy in that jet within the
 1016 electromagnetic calorimeter. When no jets fall within a cone of 0.05 of the par-
 1017 ticle, E/p and f_{EM} are both defined as zero. E/p is expected to be above 1.0
 1018 for typical SM particles because of calibration and the contributions from other
 1019 nearby particles. At these momenta there is no significant zero fraction due to
 1020 interactions with the detector or insufficient energy deposits (see Section 8.2.2).
 1021 f_{EM} is peaked close to 1.0 for electrons, and distributed between 10% and 90%
 1022 for hadrons.

1023 These trends can be seen in the two dimensional distribution for signal in
 1024 Figure 28 for stable and metastable (10 ns) events. The majority of R-Hadrons
 1025 in both samples fall into the bin for $E/p = 0$ and $f_{\text{EM}} = 0$ because the majority
 1026 of the time there is no associated jet. In the stable sample, when there often is
 1027 an associated jet, E/p is typically still below 0.1, and the f_{EM} is predominantly
 1028 under 0.8. In the metastable sample, on the other hand, E/p is larger but still
 1029 typically below 0.1 because of actual jets produced during the decay. The f_{EM} is
 1030 much lower on average in this case, below 0.1, because the 10 ns lifetime particles
 1031 rarely decay before passing through the electromagnetic calorimeter. Figure 28
 1032 also includes simulated Z decays to electrons or tau leptons. From the decays
 1033 to electrons it is clear that the majority of electrons have f_{EM} above 0.9. The
 1034 tau decays include a variety of products. Muons can be seen in the bin where
 1035 $E/p = 0$ and $f_{\text{EM}} = 0$ because they do not have an associated jet. Electrons fall
 1036 into the range where $E/p > 1$ and $f_{\text{EM}} > 0.9$. Hadronic tau decays are the most
 1037 common, and fall in the range of $0.1 < f_{\text{EM}} < 0.9$ and $E/p > 1.0$.

1038 These differences motivate an electron rejection by requiring an f_{EM} below
 1039 0.9. Similarly, isolated hadrons are rejected by requiring $E/p < 1.0$. These re-
 1040 quirements combine to remove the majority of isolated electrons and hadrons
 1041 but retain over 95% of the simulated signal across a range of masses and lifetimes.

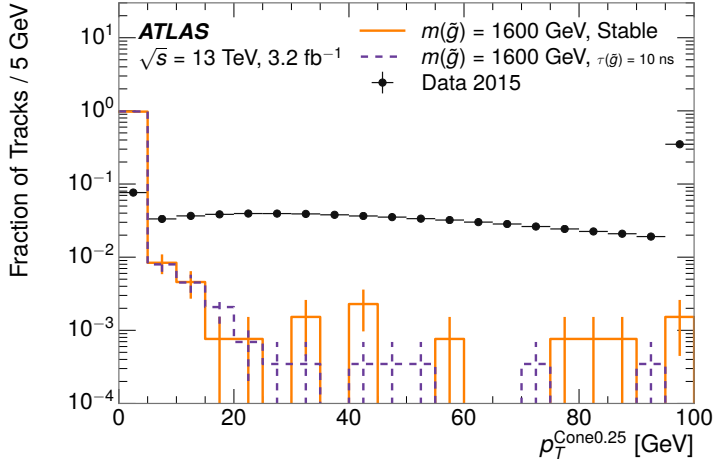


Figure 27: The distribution of summed tracked momentum within a cone of $\Delta R < 0.25$ around the candidate track for data and simulated signal events, after previous selection requirements have been applied.

1042 11.4 IONIZATION

1043 The final requirements on the candidate track are the primary discriminating
 1044 variables, the ionization in the pixel detector and the corresponding mass. That
 1045 ionization is measured in terms of dE/dx , which was shown for data and sim-
 1046 ulated signal events in Figure 24. dE/dx is dramatically greater for the high
 1047 mass signal particles than the backgrounds, which start to fall immediately af-
 1048 ter the minimally ionizing peak at $1.1 \text{ MeV g}^{-1} \text{ cm}^2$. The dE/dx for candidate
 1049 tracks must be greater than a pseudorapidity-dependent threshold, specifically
 1050 $1.80 - 0.11|\eta| + 0.17\eta^2 - 0.05\eta^3 \text{ MeV g}^{-1} \text{ cm}^{-2}$, in order to correct for an ap-
 1051 proximately 5% dependence of the MIP peak on η . The requirement was chosen
 1052 as part of the signal region optimization, and manages to reduce the backgrounds
 1053 by a factor of 100 while remaining 70-90% efficient for simulated signal events
 1054 depending on the mass.

1055 11.4.1 MASS ESTIMATION

1056 The mean value of ionization in silicon is governed by the Bethe-Bloch formula
 1057 and the most probable value follows a Landau-Vavilov distribution [36]. Those
 1058 forms inspire a parametric description of dE/dx in terms of $\beta\gamma$,

$$(dE/dx)_{\text{MPV}}(\beta\gamma) = \frac{p_1}{\beta p_3} \ln(1 + [p_2 \beta\gamma]^{p_5}) - p_4 \quad (2)$$

1059 which performs well in the range $0.3 < \beta\gamma < 1.5$. This range includes the ex-
 1060 pected range of $\beta\gamma$ for the particles targeted for this search, with $\beta\gamma \approx 2.0$ for
 1061 lower mass particles ($O(100 \text{ GeV})$) and up to $\beta\gamma \approx 0.5$ for higher mass par-
 1062 ticles ($O(1000 \text{ GeV})$). The parameters, p_i , are fit using a 2015 data sample of

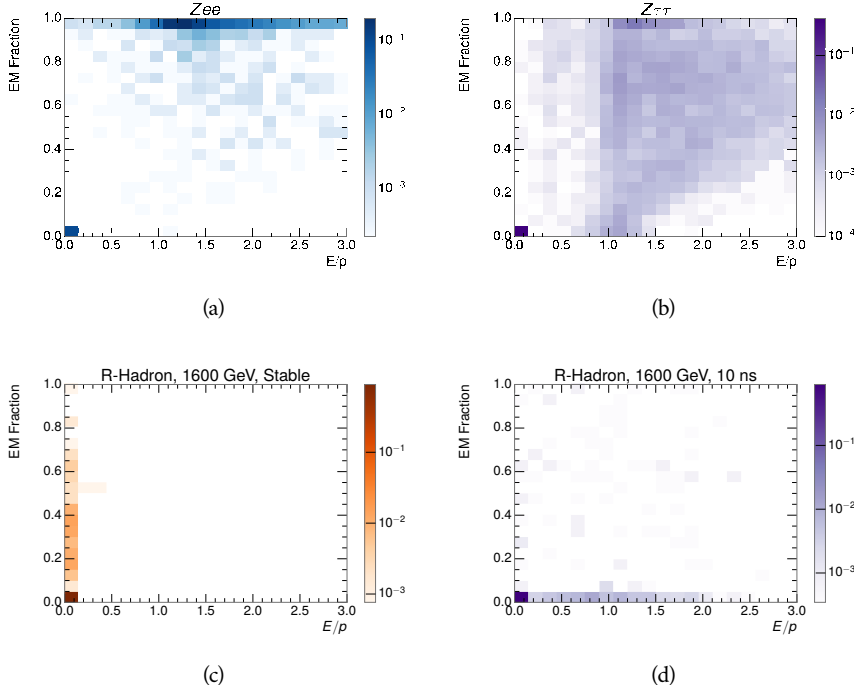


Figure 28: The normalized, two-dimensional distribution of E/p and f_{EM} for simulated (a) $Z \rightarrow ee$, (b) $Z \rightarrow \tau\tau$, (c) 1200 GeV Stable R-Hadron events, and (d) 1200 GeV, 10 ns R-Hadron events.

1063 low-momentum pions, kaons, and protons as described in Ref. [37]. Figure 29
 1064 shows the two-dimensional distribution of dE/dx and momentum along with
 1065 the above fitted values for $(dE/dx)_{\text{MPV}}$.

The above equation (2) is then numerically inverted to estimate $\beta\gamma$ and the mass for each candidate track. In simulated signal events, the mean of this mass value reproduces the generated mass up to around 1800 GeV to within 3%, and 3% shift is applied to correct for this difference. The mass distributions prior to this correction are shown for a few stable mass points in Figure 30. The large widths of these distributions come from the high variability in energy deposits in the pixel detector, but the means converge to the expected values.

This analysis evaluates expected yields and the resulting cross sectional limits using windows in this mass variable. The windows are formed by fitting mass distributions like those in Figure 30 to Gaussian distributions and taking all events that fall within $\pm 1.4\sigma$ of the mean. As can be seen in Figure 30, typical values for this width are $\sigma \approx 300 - 500$ GeV depending on the generated mass.

1078 11.5 EFFICIENCY

1079 The numbers of events passing each requirement through ionization are shown
 1080 in Table 2 for the full 2015 dataset and a simulated 1600 GeV, 10 ns lifetime R-
 1081 Hadron sample. The table highlights the overall acceptance \times efficiency for sig-
 1082 nal events, which for this example is 19%. Between SM rejection and ionization,

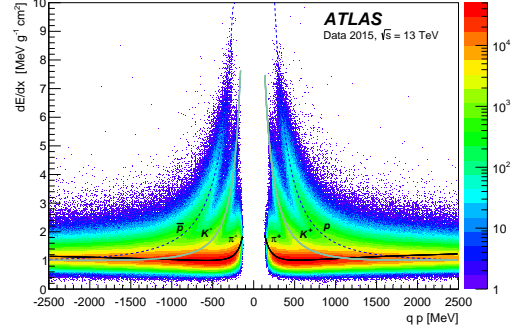


Figure 29: Two-dimensional distribution of dE/dx versus charge signed momentum (qp) for minimum-bias tracks. The fitted distributions of the most probable values for pions, kaons and protons are superimposed.

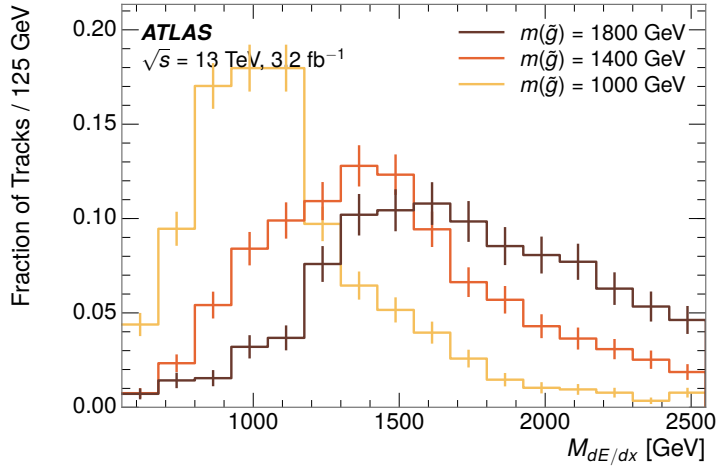


Figure 30: The distribution of mass estimated using dE/dx for simulated stable R-Hadrons with masses between 1000 and 1600 GeV.

1083 this signal region reduces the background of tracks which pass the kinematic
 1084 requirements down by an additional factor of almost 2000.

Selection	Exp. Signal Events	Observed Events in 3.2 fb^{-1}
Generated	26.0 ± 0.3	
E_T^{miss} Trigger	24.8 ± 0.3 (95%)	
$E_T^{\text{miss}} > 130 \text{ GeV}$	23.9 ± 0.3 (92%)	
Track Quality and $p_T > 50$	10.7 ± 0.2 (41%)	368324
Isolation Requirement	9.0 ± 0.2 (35%)	108079
Track $p > 150 \text{ GeV}$	6.6 ± 0.2 (25%)	47463
$M_T > 130 \text{ GeV}$	5.8 ± 0.2 (22%)	18746
Electron and Hadron Veto	5.5 ± 0.2 (21%)	3612
Muon Veto	5.5 ± 0.2 (21%)	1668
Ionization Requirement	5.0 ± 0.1 (19%)	11

Table 2: The expected number of events at each level of the selection for metastable 1600 GeV , 10 ns R-Hadrons, along with the number of events observed in data, for 3.2 fb^{-1} . The simulated yields are shown with statistical uncertainties only. The total efficiency \times acceptance is also shown for the signal.

1085 There is a strong dependence of this efficiency on lifetime and mass, with effi-
 1086 ciencies dropping to under 1% at low lifetimes. Figure 31 shows the dependence
 1087 on both mass and lifetime for all signal samples considered in this search. The
 1088 dependence on mass is relatively slight and comes predominantly from the in-
 1089 creasing fraction of R-Hadrons which pass the ionization cut with increasing
 1090 mass. The trigger and E_T^{miss} requirements are most efficient for particles that
 1091 decay before reaching the calorimeters. However, the chance of a particle to be
 1092 reconstructed as a high-quality track decreases significantly at low lifetimes as
 1093 the particle does not propagate sufficiently through the inner detector. These
 1094 effects lead to a maximum in the selection efficiency for lifetimes around 10-30
 1095 ns.

1096 The inefficiency of this signal region at short lifetimes comes almost exclu-
 1097 sively from an acceptance effect, in that the particles do not reach the necessary
 1098 layers of the SCT. This can be seen more clearly by defining a fiducial region
 1099 which includes events with at least one R-Hadron that is produced with non-
 1100 zero charge, $p_T > 50 \text{ GeV}$, $p > 150 \text{ GeV}$, $|\eta| < 2.5$, and a decay distance greater
 1101 than 37 cm in the transverse plane. At short (1 ns) lifetimes, the acceptance into
 1102 this region is as low as 4%. Once this acceptance is accounted for, the selection
 1103 efficiency ranges from 25% at lifetimes of 1 ns up to 45% at lifetimes of 10 ns.

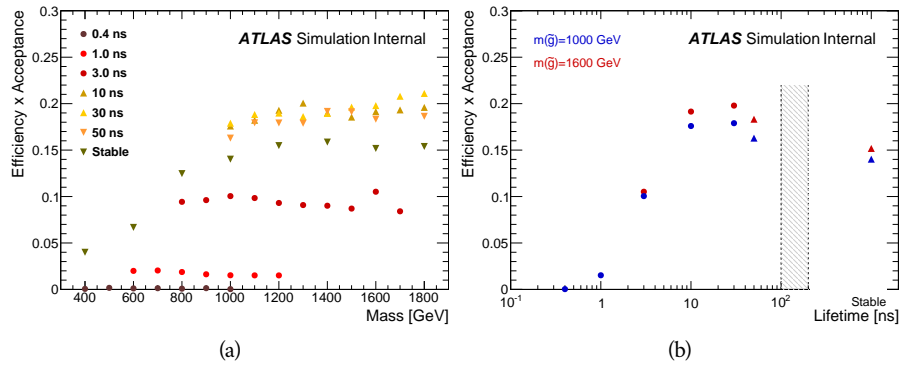


Figure 31: The acceptance \times efficiency as a function of R-Hadron (a) mass and (b) lifetime. (a) shows all of the combinations of mass and lifetime considered in this search, and (b) highlights the lifetime dependence for 1000 GeV and 1600 GeV R-Hadrons.

1104

1105 BACKGROUND ESTIMATION

1106 The event selection discussed in the previous section focuses on detector signa-
 1107 tures, emphasizing a single high-momentum, highly-ionizing track. That track
 1108 is then required to be in some way inconsistent with the expected properties
 1109 of SM particles, with various requirements designed to reject jets, hadrons,
 1110 electrons, and muons (Section 11.3). So the background for this search comes en-
 1111 tirely from reducible backgrounds that are outliers of various distributions like
 1112 dE/dx , f_{EM} , and p_T^{Cone} . The simulation can be tuned in various ways to do an
 1113 excellent job of modeling the average properties of each particle type [38], but it
 1114 is not necessarily expected to accurately reproduce outliers. For these reasons,
 1115 the background estimation used for this search is estimated entirely using data.

1116 12.1 BACKGROUND SOURCES

1117 Charged particles with lifetimes long enough to form tracks in the inner detector
 1118 can be grouped into three major categories based on their detector interactions:
 1119 hadrons, electrons, and muons. Every particle that enters into the background
 1120 for this search belongs to one of these types. Relatively pure samples of each of
 1121 these types can be formed in data by inverting the various rejection techniques
 1122 in Section 11.3. Specifically, muons are selected requiring medium muon identi-
 1123 fication, electrons requiring $E/p > 1.0$ and $f_{EM} > 0.95$, and hadrons requiring
 1124 $E/p > 1.0$ and $f_{EM} < 0.95$.

1125 Figure 32 shows the distributions of momentum and dE/dx for these cate-
 1126 gories in data, after requiring the event level selection as well as the track re-
 1127 quirements on p_T , hits, and N_{split} , as discussed in Section 11.2. Simulated signal
 1128 events are included for reference. These distribution are only illustrative of the
 1129 differences between types, as the rejection requirements could alter their shape.
 1130 This is especially significant for momentum which enters directly into E/p and
 1131 can indirectly affect muon identification. However the various types show clear
 1132 differences in both distributions. Momentum is expected to vary significantly
 1133 because of the production mechanisms for the different species. **Note for Laura:**
 1134 **Interesting that the momentum tail is so much higher for electrons than**
 1135 **muons, any idea why that would happen?** dE/dx is different between types
 1136 because of incomplete isolation; although the requirement on N_{split} helps to re-
 1137 duce the contribution of nearby particles it does not completely remove the ef-
 1138 fect of overlaps. Muons are better isolated and thus have the smallest fraction
 1139 of dE/dx above the threshold of $1.8 \text{ MeVg}^{-1}\text{cm}^2$; hadrons and electrons have
 1140 a larger fraction above this threshold.

1141 It is difficult to determine what fraction of each particle type enters into the fi-
 1142 nal signal region. The background method will not have significant dependence

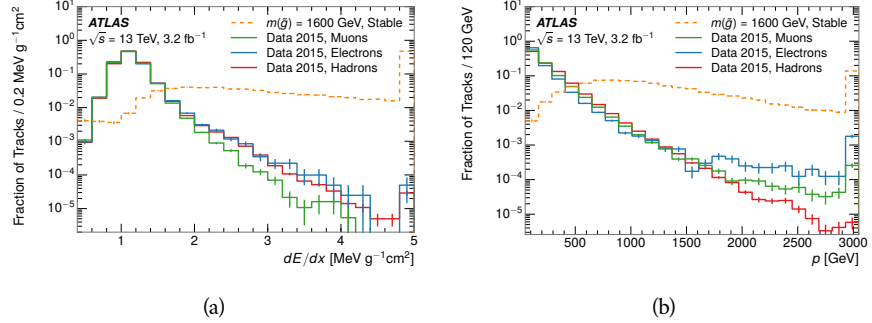


Figure 32: The distribution of (a) dE/dx and (b) momentum for tracks in data and simulated signal after requiring the event level selection and the track selection on p_T , hits, and N_{split} . Each sub-figure shows the normalized distributions for tracks classified as hadrons, electrons, and muons in data and R-Hadrons in the simulated signal.

on the relative contributions of each species, but it is useful to understand the differences between each when considering the various tests of the method.

12.2 PREDICTION METHOD

The data-driven background estimation relies on the independence of ionization and other aspects of the event. For standard model particles with momenta above 50 GeV, dE/dx is not correlated with momentum. So, the proposed method to estimate the mass distribution of the signal region is to use momentum from a track with low dE/dx (below the threshold value) and to combine it with a random dE/dx value from a dE/dx template. The resulting track is just as likely as the original, so a number of such random generations forms a distribution of mass for the signal region.

Algorithmically this method is implemented by forming two distinct Control Regions (CRs). The first CR, CR1, is formed by applying the entire event selection from Chapter 11 up to the dE/dx and mass requirements. The dE/dx requirement is instead inverted for this region. Because of the independence of dE/dx , the tracks in this control region have the same kinematic distribution as the tracks in the signal region, and are used to measure a two-dimensional template of p and η . The second CR, CR2, is formed from the event selection through the dE/dx requirement, but with an inverted E_T^{miss} requirement. The tracks in this control region are expected to have similar dE/dx distributions to the signal region, and so this region is used to measure a two-dimensional template of dE/dx and η .

The contribution of any signal to the control regions is minimized by the inverted selection requirements. Only less than 10% of simulated signal events have either dE/dx or E_T^{miss} below the threshold values in the original signal region, while the backgrounds are significantly enhanced by inverting those requirements. The signal contamination is less than 1% in both control regions for all of the simulated masses and lifetimes considered in this analysis.

With those measured templates, the shape of the mass estimation is generated by first selecting a random (p , η) combination from CR1. This momentum value is combined with a dE/dx value taken from the appropriate distribution of dE/dx for the selected η from CR2. The use of η in both random samplings controls for any correlation between p , dE/dx , and η . Those values are then used to calculate a mass in the same way that is done for regular tracks in data, see Section 11.4.1. As this procedure includes all dE/dx values, the cut at 1.8 MeVg $^{-1}$ cm 2 is then enforced to fully model the signal region. The generated mass distribution is then normalized by scaling the background estimate to the data in the region $M < 160$ GeV, where signals of this type have already been excluded [39]. This normalization takes place before the ionization requirement.

12.3 VALIDATION

The validity of the background estimation technique can be evaluated in both data and simulation. The underlying assumption that random combinations of dE/dx and momentum can predict a mass distribution in an orthogonal region can be tested using simulated samples where concerns like multiple particle types can be controlled. Using the same technique in another set of signal-depleted regions in data then extends this confidence to the more complicated case where several particle species are inherently included.

12.3.1 CLOSURE IN SIMULATION

The first test of the procedure is done using a simulated sample of $W \rightarrow \mu\nu$ decays. These types of events provide the ingredients required to test the background estimate, E_T^{miss} and isolated tracks, with high statistics. In this example there is no signal, so simulated events in the orthogonal CRs are used to estimate the shape of the mass distribution of the simulated events in the signal region. To reflect the different topology for W boson decays, the CRs use slightly modified definitions. In all CRs, the requirement of $p > 150$ GeV and the SM rejection requirements are removed. Additionally, for the signal region the requirement on E_T^{miss} is relaxed to 30 GeV and the corresponding inverted requirement on CR2 is also set at 30 GeV.

With these modified selections, the simulated and randomly generated distributions of $M_{dE/dx}$ are shown in Figure 33. This figure includes the mass distributions before and after the requirement on dE/dx , which significantly shapes the distributions. In both cases the background estimation technique reproduces the shape of $M_{dE/dx}$ in the signal region. There is a small difference in the positive tail of the mass distribution prior to the ionization cut, where the random events underestimate the fraction of tracks with mass above 150 GeV by about 20%. After the ionization requirement, however, this discrepancy is not present and the two distributions agree to within statistical uncertainties.

This ability to reproduce the shape of the mass distribution in simulated events shows that the technique works as expected. No significant biases are acquired in using low dE/dx events to select kinematic templates or in using low E_T^{miss}

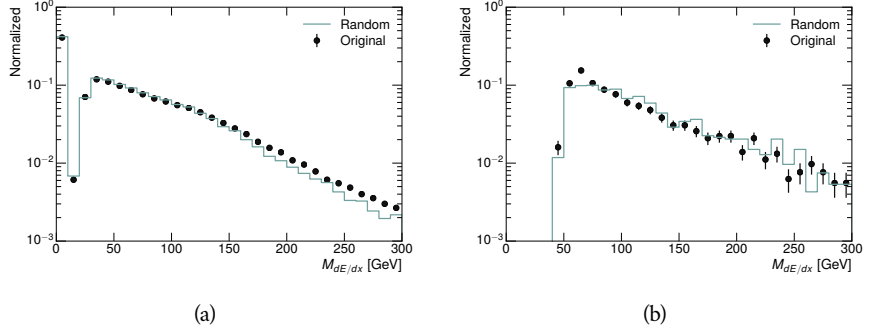


Figure 33: The distribution of $M_{dE/dx}$ (a) before and (b) after the ionization requirement for tracks in simulated W boson decays and for the randomly generated background estimate.

1213 events to select ionization templates, as either would result in a mismodeling of
1214 the shape of the mass distribution. The simulated events contain only one par-
1215 ticle type, however, so this test only establishes that the technique works well
1216 when the the CRs are populated by exactly the same species.

12.3.2 VALIDATION REGION IN DATA

The second test of the background estimate is performed using data in an orthogonal validation region. The validation region, and the corresponding CRs, are formed using the same selection requirements as in the nominal method but with a modified requirement on momentum, $50 < p[\text{GeV}] < 150$. This allows the technique to be checked in a region with very similar properties but where the signal is depleted, as the majority of the signal has momentum above 150 GeV while the backgrounds are enhanced below that threshold. Any biases on the particle composition of the CRs for the signal region will be reflected in the CRs used to estimate the mass distribution in the validation region.

Figure 34 shows the measured and randomly generated mass distributions for data before and after the ionization requirement. The background estimate does an excellent job of modeling the actual background before the ionization requirement, with good agreement to within the statistical uncertainties out to the limit of the mass distribution. There are very few events in the validation region after the ionization requirement, but the few observed events are consistent with the background prediction. The good agreement in this validation region provides a confirmation that the technique works even in the full-complexity case with multiple particle types entering the distributions. Any bias from changes in particle composition between regions is small compared to statistical uncertainties.

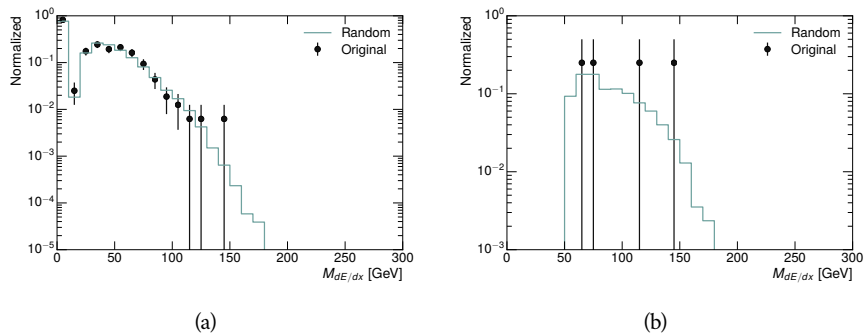


Figure 34: The distribution of $M_{dE/dx}$ (a) before and (b) after the ionization requirement for tracks in the validation region and for the randomly generated background estimate.

13

1237

1238 SYSTEMATIC UNCERTAINTIES AND RESULTS

1239 13.1 SYSTEMATIC UNCERTAINTIES

1240 13.2 FINAL YIELDS

14

1241

1242 INTERPRETATION

1243 14.1 CROSS SECTIONAL LIMITS

1244 14.2 MASS LIMITS

1245 14.3 CONTEXT FOR LONG-LIVED SEARCHES

1246

PART VI

1247

CONCLUSIONS

1248

You can put some informational part preamble text here.

15

1249

1250 SUMMARY AND OUTLOOK

1251 15.1 SUMMARY

1252 15.2 OUTLOOK

1253

PART VII

1254

APPENDIX

1255

A

1256

1257 INELASTIC CROSS SECTION

B

1258

1259 APPENDIX TEST

1260 Examples: *Italics*, SMALL CAPS, ALL CAPS ¹. Acronym testing: **UML!** (**UML!**) –
1261 **UML! – UML! (UML!) – UML!s**

This appendix is temporary and is here to be used to check the style of the document.

1262 B.1 APPENDIX SECTION TEST

1263 Random text that should take up a few lines. The purpose is to see how sections
1264 and subsections flow with some actual context. Without some body copy be-
1265 tween each heading it can be difficult to tell if the weight of the fonts, styles, and
1266 sizes use work well together.

1267 B.1.1 APPENDIX SUBECTION TEST

1268 Random text that should take up a few lines. The purpose is to see how sections
1269 and subsections flow with some actual context. Without some body copy be-
1270 tween each heading it can be difficult to tell if the weight of the fonts, styles, and
1271 sizes use work well together.

1272 B.2 A TABLE AND LISTING

1273 Curabitur tellus magna, porttitor a, commodo a, commodo in, tortor. Donec in-
1274 terdum. Praesent scelerisque. Maecenas posuere sodales odio. Vivamus metus
1275 lacus, varius quis, imperdiet quis, rhoncus a, turpis. Etiam ligula arcu, elemen-
1276 tum a, venenatis quis, sollicitudin sed, metus. Donec nunc pede, tincidunt in,
1277 venenatis vitae, faucibus vel, nibh. Pellentesque wisi. Nullam malesuada. Morbi
1278 ut tellus ut pede tincidunt porta. Lorem ipsum dolor sit amet, consectetur adip-
1279 iscing elit. Etiam congue neque id dolor.

1280 There is also a Python listing below Listing 1.

1 Footnote example.

LABITUR BONORUM PRI NO	QUE VISTA	HUMAN
fastidii ea ius	germano	demonstratea
suscipit instructior	titulo	personas
quaestio philosophia	facto	demonstrated

Table 3: Autem usu id.

1281 B.3 SOME FORMULAS

Due to the statistical nature of ionisation energy loss, large fluctuations can occur in the amount of energy deposited by a particle traversing an absorber element². Continuous processes such as multiple scattering and energy loss play a relevant role in the longitudinal and lateral development of electromagnetic and hadronic showers, and in the case of sampling calorimeters the measured resolution can be significantly affected by such fluctuations in their active layers. The description of ionisation fluctuations is characterised by the significance parameter κ , which is proportional to the ratio of mean energy loss to the maximum allowed energy transfer in a single collision with an atomic electron:

You might get unexpected results using math in chapter or section heads. Consider the pdfspacing option.

$$\kappa = \frac{\xi}{E_{\max}} \quad (3)$$

E_{\max} is the maximum transferable energy in a single collision with an atomic electron.

$$E_{\max} = \frac{2m_e\beta^2\gamma^2}{1 + 2\gamma m_e/m_x + (m_e/m_x)^2},$$

1282 where $\gamma = E/m_x$, E is energy and m_x the mass of the incident particle, $\beta^2 = 1 - 1/\gamma^2$ and m_e is the electron mass. ξ comes from the Rutherford scattering cross section and is defined as:

$$\xi = \frac{2\pi z^2 e^4 N_{Av} Z \rho \delta x}{m_e \beta^2 c^2 A} = 153.4 \frac{z^2}{\beta^2} \frac{Z}{A} \rho \delta x \text{ keV},$$

1285 where

- z charge of the incident particle
- N_{Av} Avogadro's number
- Z atomic number of the material
- A atomic weight of the material
- ρ density
- δx thickness of the material
- 1287 κ measures the contribution of the collisions with energy transfer close to
1288 E_{\max} . For a given absorber, κ tends towards large values if δx is large and/or if
1289 β is small. Likewise, κ tends towards zero if δx is small and/or if β approaches
1290 1.

2 Examples taken from Walter Schmidt's great gallery:
<http://home.vrweb.de/~was/mathfonts.html>

Listing 1: A floating example (listings manual)

```
1 for i in xrange(10):
    print i, i*i, i*i*i
print "done"
```

1291 The value of κ distinguishes two regimes which occur in the description of
1292 ionisation fluctuations:

- 1293 1. A large number of collisions involving the loss of all or most of the incident
1294 particle energy during the traversal of an absorber.

1295 As the total energy transfer is composed of a multitude of small energy
1296 losses, we can apply the central limit theorem and describe the fluctua-
1297 tions by a Gaussian distribution. This case is applicable to non-relativistic
1298 particles and is described by the inequality $\kappa > 10$ (i. e., when the mean en-
1299 ergy loss in the absorber is greater than the maximum energy transfer in
1300 a single collision).

- 1301 2. Particles traversing thin counters and incident electrons under any condi-
1302 tions.

1303 The relevant inequalities and distributions are $0.01 < \kappa < 10$, Vavilov
1304 distribution, and $\kappa < 0.01$, Landau distribution.

1305 BIBLIOGRAPHY

- 1306 [1] S. Agostinelli et al. “GEANT4: A simulation toolkit”. In: *Nucl. Instrum. Meth.*
1307 A 506 (2003), pp. 250–303. doi: [10.1016/S0168-9002\(03\)01368-8](https://doi.org/10.1016/S0168-9002(03)01368-8).
- 1308 [2] ATLAS Collaboration. “A study of the material in the ATLAS inner de-
1309 tector using secondary hadronic interactions”. In: *JINST* 7 (2012), P01013.
1310 doi: [10.1088/1748-0221/7/01/P01013](https://doi.org/10.1088/1748-0221/7/01/P01013). arXiv: [1110.6191 \[hep-ex\]](https://arxiv.org/abs/1110.6191).
1311 [PERF-2011-08](#).
- 1312 [3] ATLAS Collaboration. “Electron and photon energy calibration with the
1313 ATLAS detector using LHC Run 1 data”. In: *Eur. Phys. J. C* 74 (2014), p. 3071.
1314 doi: [10.1140/epjc/s10052-014-3071-4](https://doi.org/10.1140/epjc/s10052-014-3071-4). arXiv: [1407.5063](https://arxiv.org/abs/1407.5063)
1315 [hep-ex]. [PERF-2013-05](#).
- 1316 [4] ATLAS Collaboration. “A measurement of the calorimeter response to sin-
1317 ggle hadrons and determination of the jet energy scale uncertainty using
1318 LHC Run-1 $p\bar{p}$ -collision data with the ATLAS detector”. In: (2016). arXiv:
1319 [1607.08842 \[hep-ex\]](https://arxiv.org/abs/1607.08842). [PERF-2015-05](#).
- 1320 [5] ATLAS Collaboration. “Single hadron response measurement and calorime-
1321 ter jet energy scale uncertainty with the ATLAS detector at the LHC”. In:
1322 *Eur. Phys. J. C* 73 (2013), p. 2305. doi: [10.1140/epjc/s10052-013-2305-1](https://doi.org/10.1140/epjc/s10052-013-2305-1). arXiv: [1203.1302 \[hep-ex\]](https://arxiv.org/abs/1203.1302). [PERF-2011-05](#).
- 1324 [6] ATLAS Collaboration. “The ATLAS Simulation Infrastructure”. In: *Eur.*
1325 *Phys. J. C* 70 (2010), p. 823. doi: [10.1140/epjc/s10052-010-1429-9](https://doi.org/10.1140/epjc/s10052-010-1429-9).
1326 arXiv: [1005.4568 \[hep-ex\]](https://arxiv.org/abs/1005.4568). [SOFT-2010-01](#).
- 1327 [7] T. Sjöstrand, S. Mrenna, and P. Skands. “A Brief Introduction to PYTHIA
1328 8.1”. In: *Comput. Phys. Commun.* 178 (2008), pp. 852–867. doi: [10.1016/j.cpc.2008.01.036](https://doi.org/10.1016/j.cpc.2008.01.036). arXiv: [0710.3820](https://arxiv.org/abs/0710.3820).
- 1330 [8] ATLAS Collaboration. *Summary of ATLAS Pythia 8 tunes*. ATL-PHYS-PUB-
1331 2012-003. 2012. URL: <http://cds.cern.ch/record/1474107>.
- 1332 [9] A.D. Martin, W.J. Stirling, R.S. Thorne, and G. Watt. “Parton distributions
1333 for the LHC”. In: *Eur. Phys. J. C* 63 (2009). Figures from the [MSTW Website](#),
1334 pp. 189–285. doi: [10.1140/epjc/s10052-009-1072-5](https://doi.org/10.1140/epjc/s10052-009-1072-5). arXiv: [0901.0002](https://arxiv.org/abs/0901.0002).
- 1336 [10] A. Sherstnev and R.S. Thorne. “Parton Distributions for LO Generators”.
1337 In: *Eur. Phys. J. C* 55 (2008), pp. 553–575. doi: [10.1140/epjc/s10052-008-0610-x](https://doi.org/10.1140/epjc/s10052-008-0610-x). arXiv: [0711.2473](https://arxiv.org/abs/0711.2473).
- 1339 [11] A. Ribon et al. *Status of Geant4 hadronic physics for the simulation of LHC*
1340 *experiments at the start of LHC physics program*. CERN-LCGAPP-2010-02.
1341 2010. URL: <http://lcgapp.cern.ch/project/docs/noteStatusHadronic2010.pdf>.

- 1343 [12] M. P. Guthrie, R. G. Alsmiller, and H. W. Bertini. "Calculation of the cap-
 1344 ture of negative pions in light elements and comparison with experiments
 1345 pertaining to cancer radiotherapy". In: *Nucl. Instrum. Meth.* 66 (1968), pp. 29–
 1346 36. doi: [10.1016/0029-554X\(68\)90054-2](https://doi.org/10.1016/0029-554X(68)90054-2).
- 1347 [13] H. W. Bertini and P. Guthrie. "News item results from medium-energy
 1348 intranuclear-cascade calculation". In: *Nucl. Instr. and Meth. A* 169 (1971),
 1349 p. 670. doi: [10.1016/0375-9474\(71\)90710-X](https://doi.org/10.1016/0375-9474(71)90710-X).
- 1350 [14] V.A. Karmanov. "Light Front Wave Function of Relativistic Composite
 1351 System in Explicitly Solvable Model". In: *Nucl. Phys. B* 166 (1980), p. 378.
 1352 doi: [10.1016/0550-3213\(80\)90204-7](https://doi.org/10.1016/0550-3213(80)90204-7).
- 1353 [15] H. S. Fesefeldt. *GHEISHA program*. Pitha-85-02, Aachen. 1985.
- 1354 [16] G. Folger and J.P. Wellisch. "String parton models in Geant4". In: (2003).
 1355 arXiv: [nucl-th/0306007](https://arxiv.org/abs/nucl-th/0306007).
- 1356 [17] N. S. Amelin et al. "Transverse flow and collectivity in ultrarelativistic
 1357 heavy-ion collisions". In: *Phys. Rev. Lett.* 67 (1991), p. 1523. doi: [10.1103/PhysRevLett.67.1523](https://doi.org/10.1103/PhysRevLett.67.1523).
- 1359 [18] N. S. Amelin et al. "Collectivity in ultrarelativistic heavy ion collisions". In:
 1360 *Nucl. Phys. A* 544 (1992), p. 463. doi: [10.1016/0375-9474\(92\)90598-E](https://doi.org/10.1016/0375-9474(92)90598-E).
- 1362 [19] L. V. Bravina et al. "Fluid dynamics and Quark Gluon string model - What
 1363 we can expect for Au+Au collisions at 11.6 AGeV/c". In: *Nucl. Phys. A* 566
 1364 (1994), p. 461. doi: [10.1016/0375-9474\(94\)90669-6](https://doi.org/10.1016/0375-9474(94)90669-6).
- 1365 [20] L. V. Bravin et al. "Scaling violation of transverse flow in heavy ion colli-
 1366 sions at AGS energies". In: *Phys. Lett. B* 344 (1995), p. 49. doi: [10.1016/0370-2693\(94\)01560-Y](https://doi.org/10.1016/0370-2693(94)01560-Y).
- 1368 [21] B. Andersson et al. "A model for low-pT hadronic reactions with general-
 1369 izations to hadron-nucleus and nucleus-nucleus collisions". In: *Nucl. Phys.*
 1370 *B* 281 (1987), p. 289. doi: [10.1016/0550-3213\(87\)90257-4](https://doi.org/10.1016/0550-3213(87)90257-4).
- 1371 [22] B. Andersson, A. Tai, and B.-H. Sa. "Final state interactions in the (nuclear)
 1372 FRITIOF string interaction scenario". In: *Z. Phys. C* 70 (1996), pp. 499–
 1373 506. doi: [10.1007/s002880050127](https://doi.org/10.1007/s002880050127).
- 1374 [23] B. Nilsson-Almqvist and E. Stenlund. "Interactions Between Hadrons and
 1375 Nuclei: The Lund Monte Carlo, Fritiof Version 1.6". In: *Comput. Phys. Com-*
 1376 *mun.* 43 (1987), p. 387. doi: [10.1016/0010-4655\(87\)90056-7](https://doi.org/10.1016/0010-4655(87)90056-7).
- 1377 [24] B. Ganhuyag and V. Uzhinsky. "Modified FRITIOF code: Negative charged
 1378 particle production in high energy nucleus nucleus interactions". In: *Czech.*
 1379 *J. Phys.* 47 (1997), pp. 913–918. doi: [10.1023/A:1021296114786](https://doi.org/10.1023/A:1021296114786).
- 1380 [25] ATLAS Collaboration. "Topological cell clustering in the ATLAS calorime-
 1381 ters and its performance in LHC Run 1". In: (2016). arXiv: [1603.02934](https://arxiv.org/abs/1603.02934)
 1382 [[hep-ex](#)].
- 1383 [26] Peter Speckmayer. "Energy Measurement of Hadrons with the CERN AT-
 1384 LAS Calorimeter". Presented on 18 Jun 2008. PhD thesis. Vienna: Vienna,
 1385 Tech. U., 2008. URL: <http://cds.cern.ch/record/1112036>.

- 1386 [27] CMS Collaboration. “The CMS barrel calorimeter response to particle
1387 beams from 2 to 350 GeV/c”. In: *Eur. Phys. J. C* 60.3 (2009). doi: [10.1140/epjc/s10052-009-0959-5](https://doi.org/10.1140/epjc/s10052-009-0959-5).
- 1389 [28] J. Beringer et al. (Particle Data Group). “Review of Particle Physics”. In:
1390 *Chin. Phys. C* 38 (2014), p. 090001. URL: <http://pdg.lbl.gov>.
- 1391 [29] P. Adragna et al. “Measurement of Pion and Proton Response and Lon-
1392 gitudinal Shower Profiles up to 20 Nuclear Interaction Lengths with the
1393 ATLAS Tile Calorimeter”. In: *Nucl. Instrum. Meth. A* 615 (2010), pp. 158–
1394 181. doi: [10.1016/j.nima.2010.01.037](https://doi.org/10.1016/j.nima.2010.01.037).
- 1395 [30] ATLAS Collaboration. “Jet energy measurement and its systematic uncer-
1396 tainty in proton–proton collisions at $\sqrt{s} = 7$ TeV with the ATLAS detec-
1397 tor”. In: *Eur. Phys. J. C* 75 (2015), p. 17. doi: [10.1140/epjc/s10052-014-3190-y](https://doi.org/10.1140/epjc/s10052-014-3190-y). arXiv: [1406.0076 \[hep-ex\]](https://arxiv.org/abs/1406.0076). PERF-2012-01.
- 1399 [31] Hung-Liang Lai, Marco Guzzi, Joey Huston, Zhao Li, Pavel M. Nadolsky,
1400 et al. “New parton distributions for collider physics”. In: *Phys. Rev. D* 82
1401 (2010), p. 074024. doi: [10.1103/PhysRevD.82.074024](https://doi.org/10.1103/PhysRevD.82.074024). arXiv: [1007.2241 \[hep-ph\]](https://arxiv.org/abs/1007.2241).
- 1403 [32] E. Abat et al. “Study of energy response and resolution of the ATLAS barrel
1404 calorimeter to hadrons of energies from 20 to 350 GeV”. In: *Nucl. Instrum.*
1405 *Meth. A* 621.1-3 (2010), pp. 134 – 150. doi: <http://dx.doi.org/10.1016/j.nima.2010.04.054>.
- 1407 [33] ATLAS Collaboration. “Jet energy measurement with the ATLAS detector
1408 in proton–proton collisions at $\sqrt{s} = 7$ TeV”. In: *Eur. Phys. J. C* 73 (2013),
1409 p. 2304. doi: [10.1140/epjc/s10052-013-2304-2](https://doi.org/10.1140/epjc/s10052-013-2304-2). arXiv: [1112.6426 \[hep-ex\]](https://arxiv.org/abs/1112.6426). PERF-2011-03.
- 1411 [34] ATLAS Collaboration. “Search for heavy long-lived charged R -hadrons
1412 with the ATLAS detector in 3.2 fb^{-1} of proton–proton collision data at
1413 $\sqrt{s} = 13$ TeV”. In: *Phys. Lett. B* 760 (2016), pp. 647–665. doi: [10.1016/j.physletb.2016.07.042](https://doi.org/10.1016/j.physletb.2016.07.042). arXiv: [1606.05129 \[hep-ex\]](https://arxiv.org/abs/1606.05129).
- 1415 [35] A. C. Kraan, J. B. Hansen, and P. Nevski. “Discovery potential of R-hadrons
1416 with the ATLAS detector”. In: *Eur. Phys. J. C* 49 (2007), pp. 623–640. doi:
1417 [10.1140/epjc/s10052-006-0162-x](https://doi.org/10.1140/epjc/s10052-006-0162-x). arXiv: [hep-ex/0511014 \[hep-ex\]](https://arxiv.org/abs/hep-ex/0511014).
- 1419 [36] K. A. Olive et al. “Review of Particle Physics”. In: *Chin. Phys. C* 38 (2014),
1420 p. 090001. doi: [10.1088/1674-1137/38/9/090001](https://doi.org/10.1088/1674-1137/38/9/090001).
- 1421 [37] “dE/dx measurement in the ATLAS Pixel Detector and its use for particle
1422 identification”. In: (2011).
- 1423 [38] ATLAS Collaboration. “The ATLAS Simulation Infrastructure”. In: *Eur.*
1424 *Phys. J. C* 70 (2010), pp. 823–874. doi: [10.1140/epjc/s10052-010-1429-9](https://doi.org/10.1140/epjc/s10052-010-1429-9). arXiv: [1005.4568 \[physics.ins-det\]](https://arxiv.org/abs/1005.4568).

- 1426 [39] ATLAS Collaboration. “Search for metastable heavy charged particles with
1427 large ionisation energy loss in $p\bar{p}$ collisions at $\sqrt{s} = 8$ TeV using the AT-
1428 LAS experiment”. In: *Eur. Phys. J. C* 75 (2015), p. 407. doi: [10.1140/epjc/s10052-015-3609-0](https://doi.org/10.1140/epjc/s10052-015-3609-0). arXiv: [1506.05332 \[hep-ex\]](https://arxiv.org/abs/1506.05332). SUSY-
1429 2014-09.
1430

1431 DECLARATION

1432 Put your declaration here.

1433 *Berkeley, CA, September 2016*

1434

Bradley Axen

1435

1436 COLOPHON

1437

Not sure that this is necessary.